Article:
Kumar Borah, P, Sundar Das, A, Mukhopadhyay, R et al. (2 more authors) (2020) Macromolecular design of folic acid functionalized amylopectin- albumin core-shell nanogels for improved physiological stability and colon cancer cell targeted delivery of curcumin. Journal of Colloid and Interface Science, 580. pp. 561-572. ISSN 0021-9797

https://doi.org/10.1016/j.jcis.2020.07.056

Macromolecular design of folic acid functionalized amylopectin-albumin core-shell nanogels for improved physiological stability and colon cancer cell targeted delivery of curcumin

Pallab Kumar Borah[a, b], Anindhya Sundar Das[c], Rupak Mukhopadhyay[c], Anwesha Sarkar[b]†, Raj Kumar Duary[a]*

[a] *Department of Food Engineering and Technology, School of Engineering, Tezpur University, 784 028, India*

[b] *Food Colloids and Bioprocessing Group, School of Food Science and Nutrition, University of Leeds, LS2 9JT, United Kingdom*

[c] *Department of Molecular Biology and Biotechnology, School of Sciences, Tezpur University, 784 028, India*

Email addresses: pallab@tezu.ernet.in; dasanindhyasundar@gmail.com; mrupak@tezu.ernet.in; A.Sarkar@leeds.ac.uk†; duary@tezu.ernet.in*

Corresponding author

* Dr. Raj Kumar Duary, E-mail address: duary@tezu.ernet.in; rkduary@gmail.com, Phone: +91(0)-3712-275709.

Joint corresponding author

† Dr. Anwesha Sarkar, E-mail address: A.Sarkar@leeds.ac.uk, Phone: +44(0)-113-343-2748.

Graphical abstract

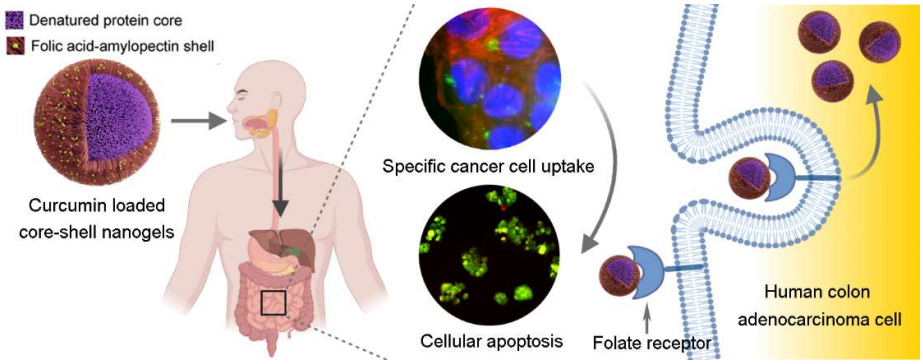

Abstract

Nanogels have potential for encapsulating cancer therapeutics, yet their susceptibility to physiological degradation and lack of cellular specificity hinder their use as effective oral delivery vehicles. Herein, we engineered novel albumin-core with folic acid functionalized hyperbranched amylopectin shell-type nanogels, prepared through a two-step reaction and loaded with curcumin while the proteinaceous core was undergoing thermal gelation. The nanogels had a mean hydrodynamic diameter of ca. 90 nm and ζ-potential of ca. -24 mV. Encapsulation of curcumin within the nanogels was restored, up to ca. 0.05 mg mL^{-1}, beyond which, a gradual increase in size and a decrease in ζ-potential was observed. The core-shell structures were resilient to *in vitro* physiological oral-gastrointestinal digestion owing to a liquid crystalline B- and V-type polymorphism in the polysaccharide shell, the latter being driven by the shell functionalization with folic acid. Additionally, these biocompatible nanogels restored stability of the encapsulated curcumin and exhibited augmented cellular uptake and retention specifically in folate receptor-positive HT29 human colon adenocarcinoma cells, inducing early-stage apoptosis. Novel insights from this study represent a promising platform for rational designing of future oral delivery systems that can surmount physiological barriers for delivering cancer therapeutics to colon cancer cells with improved stability and specificity.

Keywords

Albumin; Amylopectin starch; Core-shell nanogels; Colon cancer therapy; Curcumin encapsulation; Folic acid; Improved bioavailability; *in vitro* Digestion; Maillard reaction; Targeted oral drug delivery.

Abbreviations

ACS, amylopectin from corn starch; SF20, folic acid functionalized amylopectin polymers; BSA_{native}, native bovine serum albumin; BSA, nanogels derived from BSA_{native}; BSA_{cur}, curcumin encapsulated BSA; BSA_{FITC}, FITC tagged BSA; BSM_{con}, Maillard conjugates of bovine serum albumin + SF20; BSM, nanogels derived from BSM_{con}; BSM_{cur}, curcumin encapsulated BSM; BSM_{FITC}, FITC tagged BSM; BAM_{con}, Maillard conjugates of bovine serum albumin + ACS; BAM, nanogels derived from BAM_{con}; BAM_{cur}, curcumin encapsulated BAM; BAM_{FITC}, FITC tagged BAM; D_h, mean hydrodynamic diameter; KDa, Kilodalton; wt. %, weight percentage; vol. %, volume percentage.

1. Introduction

Colon cancer is one of the most pervasive malignant cancers in existence [1]. To ameliorate such cancers, tremendous advances in nanotechnology research have facilitated a steep rise in fabricating nano-carriers (ranging from ~ 1 to 100 nm) for localized delivery of cancer therapeutics [2]. Such nano-carriers can be beneficial over direct administration of the bare cancer drugs as they are aimed to package the cancer therapeutic and deliver them to the targeted cancer tissues with improved pharmacokinetic and pharmacodynamic outcomes [3, 4]. By exploiting biodegradable chemistries, nano-carriers with reduced cytotoxicity as compared to the synthetic polymeric counterparts have ranged in literature from micelles, liposomes, solid lipid nanoparticles, dendrimers, to nanogels.

Nanogels, *i.e.* nanometric-sized hydrogels are considered as one of the most promising classes of nanoparticle-based delivery vehicles as it combines properties of both the hydrogels and the nanoparticles [5]. Furthermore, nanogels are tunable in size, surface properties, responsiveness, *etc.* for cancer cell targeting [5]. In particular, nanogels synthesized from proteins [6-8], including bovine serum albumin (BSA), which is a natural transporter of small-molecule hydrophobes [9], have recently attracted a great deal of research attention for therapeutic delivery. The major advantages of protein-based nanogels are their biodegradability, biocompatibility, and non-antigenicity along with flexibility for surface modifications and/or chemical functionalization [8, 10]. Additionally, proteins are polyampholytic in nature and enhanced surface hydrophobicity of thermally-treated globular proteins due to unfolding offers these protein-based nanogels to serve as excellent carriers for hydrophobic and charged therapeutic molecules [9, 11-14]. However, most protein-based nanogels suffer from high susceptibility to proteolytic enzymes during physiological transit [10, 15, 16] which may consequently result in structural degradation. This might result in

premature therapeutic release during oral delivery or even degradation of the therapeutic before reaching the targeted diseased colonic sites.

To address this afore-mentioned challenge of physiological degradation, covalent conjugation of proteins with polysaccharides can be particularly appealing [9, 14, 17]. Usually, protein-polysaccharide conjugates are developed *via* Maillard dry-heat reaction [17] resulting in the formation of a copolymer conjugate between the reducing end carbonyl group in the polysaccharides and the ε-amino groups in the protein [18]. This can be followed by the employment of a thermal-gelation process to prepare nanogels that result in a sophisticated core-shell structure [18, 19]. The protein core is known to act as a hydrophobic carrier for encapsulating hydrophobic therapeutic molecules and safeguard the latter against physiological degradation, whereas the polysaccharide shell provides a steric barrier for limiting the digestion of the proteinaceous core [17]. Yet, such nanogel architecture lacks cellular specificity, and indiscriminately delivers the therapeutics to both diseased and healthy cells. This not only reduces the bioavailability of the therapeutics at diseased sites but also promote undesired side effects upon oral administration.

These issues can be addressed using cancer cell-specific delivery of therapeutic molecules using core-shell nanogel architectures equipped with targeting moieties [20, 21]. The polysaccharides shells provide spatial positioning of functional groups for attachment of targeting moieties, such as the vitamin B9 *i.e.* folic acid ((2S)-2-[[4-[(2-amino-4-oxo-3H-pteridin-6-yl)methylamino]benzoyl]amino]pentanedioic acid; PubChem CID: 135398658). Folic acid is known to impart specific as well as high binding affinity (K_d, ca. 10^{-7} mM) to folate receptors, the latter are overexpressed ca. 100 - 300 times greater in a vast majority of cancer cells including the colon [22]. Additionally, experimental studies coupled with computational simulations have shown that folic acid can inhibit a wide array of digestive enzymes such as α-amylase, pepsin, and trypsin [23, 24]. Our group has recently developed

folic acid functionalized amylopectin (SF20) polymers and deciphered its structural hierarchy using small angle and wide angle X-ray scattering and we demonstrated a high degree of resilience of these designed polymers to physiological digestion [22, 25]. The glucose homopolymers, amylopectin, offers significant advantages in terms of larger spatial conformation for folic acid-functionalization owing to its branched tree-like topology [26]. Such advantages are deficient in linear polysaccharides, such as dextran, chitosan, and hydroxyethyl cellulose that are currently utilized in most drug delivery studies to date [27].

Herein, we report the design of novel folic acid functionalized core-shell nanogels and hypothesize that the vehicle will uniquely combine 1) biocompatibility, 2) restricted degradation of the delivery vehicle and payload in *in vitro* physiological conditions, and 3) targeted colon cancer cell specificity and retention. The nanogels functionalized with folic acid are expected to have a two-fold beneficial effect. Firstly, folic acid is expected to serve as a targeting motif for specific recognition, cellular-uptake, and retention in folate receptor-positive colon cancer cells. This in turn can increase the bioavailability of the encapsulated therapeutics specifically in the diseased cells without interfering with the healthy cells, thus providing an oral targeted delivery, which is seldom reported in the literature. Curcumin ((1E,6E)-1,7-bis(4-hydroxy-3-methoxyphenyl)hepta-1,6-diene-3,5-dione; PubChem CID: 969516), a highly hydrophobic polyphenol derived from turmeric (*Curcuma longa*) was chosen as a model cancer therapeutics in this study owing to its well-established pharmacological properties and high responsiveness to physiological degradation [4, 28, 29]. Secondly, this is the first study where folic acid is additionally utilized to drive a liquid crystalline polymorphism in the polysaccharide chains of the shell, which is expected to hinder the physiological degradation of the nanogels and enhance their stability in the complex oral-to-gastrointestinal milieu.

In this study, we systematically deconvoluted the structure of the nanogels using dynamic/ static light scattering, electrophoretic mobility, X-ray diffraction, spectroscopy (circular dichroism and infrared), thermogravimetric analysis, and microscopy (fluorescence and scanning-/transmission-electron microscopy) at multiple length scales. Then, we discuss the unprecedented bio-functional properties of these nanogels loaded with curcumin in terms of *in vitro* physiological stability, alongside specific internalization and inhibition of folate-receptor positive human cellular models of colon cancer. Novel insights from this study can be used to inform future design of oral delivery vehicles that are biocompatible, physiologically stable, and allow targeting the cancer therapeutics specifically to the colon cancer cell.

2. Materials and methods

2.1. Materials

Bovine serum albumin (BSA, ≥ 96 %), amylopectin from corn starch (ACS, containing no amylose as assessed using colorimetric procedure [22]), folic acid (FA, ≥ 97 %), curcumin from *Curcuma longa* (≥ 81 %), 1, 3-dicyclohexylcarbodiimide (*N*,*N*'-dicyclohexylmethanediimine, DCC, ≥ 99 %), 4-dimethylaminopyridine (*N*,*N*-dimethylpyridin-4-amine, DMAP, ≥ 99 %), potassium bromide (KBr, ≥ 99 %), *n*-hexane (≥ 97 %), α-amylase type IX-A from human saliva (300 - 1500 U mg^{-1}), α-amylase type VI-B from porcine pancreas (> 10 U mg^{-1}), pepsin from porcine gastric mucosa (3200 - 4500 U mg^{-1}), pancreatin from porcine pancreas (4 × USP), toluene (≥ 99.8 %), isopropanol (≥ 70 % in H_2O), hydrochloric acid (HCl, 36.5 - 38.0 %), dimethyl sulfoxide **(**DMSO, ≥ 99.9 %) sodium hydroxide (NaOH, ≥ 97 %), *O*-phthaldialdehyde reagent (phthaldialdehyde (1 mg mL^{-1}), Brij® 35, methanol, 2-mercaptoethanol, potassium hydroxide, and boric acid, pH 10.4), fluorescein isothiocyanate isomer I (FITC, ≥ 90 %), TERGITOL™ Type NP-40**,** and Amicon® Ultra

centrifugal dialysis filter (30 kDa MWCO) were purchased from Sigma-Aldrich, India or UK. The HT29 (folate receptor-positive human colon adenocarcinoma) and A549 (folate receptor-negative human alveolar carcinoma) cells were purchased from the National Centre for Cell Science, India. ProLong™ Gold Antifade Mountant with 4′, 6-diamidino-2-phenylindole (DAPI) was purchased from Thermo Fischer Scientific, India. Alexa Fluor™ 568 Phalloidin, fetal bovine serum (FBS), and antibiotics (100 unit mL^{-1} penicillin and 100 µg mL^{-1} streptomycin) were purchased from Abcam, USA. 3-(4, 5-dimethyl-2-thiazolyl)-2, 5-diphenyl-2H-tetrazolium bromide (MTT), Dulbecco's Modified Eagle Medium (DMEM), Dulbecco's Phosphate Buffered Saline (DPBS), acridine orange (AO), and ethidium bromide (EB) were purchased from Himedia Labs, India. Milli-Q water (Millipore Corp., USA) was used throughout the experiments (18.2 MΩ.cm ionic purity at 25 °C).

The folic acid functionalized amylopectin (SF20) polymer with a degree of substitution, 0.02; *i.e.* 0.02 folic acid molecules per glucose residues of the ACS polymer was synthesized as described in detail previously [22]. Briefly, folic acid was reacted with DCC and DMAP (FA: DCC: DMAP molar ratio of 1:1:0.3) by stirring for 30 min in DMSO. ACS was added to the reaction mixture (20 wt. % of folic acid to starch dry weight) and was further reacted under dark conditions for 24 h at 30 °C. The reaction products were washed with 100 mM HCl and water, and then dialyzed (3.5 kDa MWCO) against 10 mM phosphate buffer at pH 7.4 containing 100 mM NaCl for 24 h, and, then with water for another 24 h. The product was lyophilized, ground to a fine powder, and the SF20 polymer was obtained. The substitution of folic acid in SF20 is described using complementary spectroscopy (UV and infrared) and confocal laser scanning microscopy elsewhere [22].

2.2. Synthesis of albumin (BSA)-folic acid functionalized amylopectin (SF20) copolymer conjugates

Maillard reaction was used to conjugate BSA and SF20 using a molar ratio of 1:1, lysine residues of BSA: SF20 [30]. Both BSA and SF20 were dissolved together in 10 mM phosphate buffer and the pH of the mixture was adjusted to pH 8.0 using NaOH. The mixture was then stirred at 500 rpm for 12 h in the dark at room temperature. The resultant dispersion was lyophilized and then reacted inside a desiccator pre-conditioned using a saturated solution of KBr to yield 79 % relative humidity at 60 °C. This BSA + SF20 Maillard copolymer conjugate was denoted as BSM_{con} henceforth. The conjugation degree of the conjugate was analyzed by sodium dodecyl sulfate-polyacrylamide gel electrophoresis (SDS-PAGE) at a protein load of 10 µg $well^{-1}$ and *O*-phthaldialdehyde (OPA) assay as described elsewhere [31]. Additionally, Fourier transform infrared (FTIR) spectra (4500 - 400 cm^{-1}, where 32 scans were averaged with a resolution of 2 cm^{-1}) of the conjugates were obtained. Samples were prepared as KBr pellets and scanned against air background on a Spectrum 100 ATR-FTIR Spectrometer (Perkin Elmer Inc., USA) with KBr correction optics.

Control groups included BSA + ACS Maillard copolymer conjugate (BAM_{con}) without any addition of folic acid groups produced under the same reaction conditions and native bovine serum albumin (BSA_{native}) protein.

2.3. Fabrication of nanogels and curcumin encapsulation

BSM_{con} (1 mg mL^{-1}) was stirred in 10 mM phosphate buffer at 500 rpm for 12 h using a magnetic stirrer for complete hydration. For clarity, only the concentration of albumin in the protein-polysaccharide conjugates is denoted. The nanogels were prepared as described earlier by Fan et al. [31] with some modifications. Briefly, the hydrated dispersion of BSM_{con} prepared above was heated to 80 °C. To load curcumin, the latter was dissolved in ethanol and added to the hydrated dispersion of copolymer conjugates at various loads (0 - 0.2 mg mL^{-1}). Ethanol concentration in the final mixture was < 0.01 %. The thermal treatment was continued alongside stirring at 500 rpm for 60 min and then allowed to cool to room

temperature to produce curcumin encapsulated thermally-crosslinked nanogels. Nanogel fabrication was always carried out in dark conditions and stored at 4 °C before use. Any minor precipitation of copolymer conjugate or curcumin if observed was centrifuged out of the dispersion at 3000 *g* for 10 mins. The nanogels without curcumin (0 mg mL^{-1})/with curcumin (0.02 - 0.2 mg mL^{-1}) were denoted as BSM/BSM_{cur}, respectively. Control nanogels without folic acid or any conjugation with ACS were denoted as BAM and BSA (without curcumin) and BAM_{cur} and BSA_{cur} (with curcumin), respectively. Curcumin encapsulation efficiency (*CEE*, indicating the mass % of loaded curcumin that was encapsulated into the nanogels) and the curcumin loading efficiency (*CLE*, indicating the mass % of the nanogels comprising the encapsulated curcumin) were expressed as described previously [32]:

$$CEE(\%) = \frac{M_T - M_P}{M_T} \times 100 \quad \text{Eq. (1)}$$

$$CLE\ (\%) = \frac{M_T - M_P}{(M_T - M_P) + p} \times 100 \quad \text{Eq. (2)}$$

where M_T, M_P, and p represent the mass of the total curcumin load, the curcumin in the precipitate, and the total weight of the polymer, respectively. Absorbance was measured at 420 nm.

2.4. Characterization of the nanogels

2.4.1. Mean hydrodynamic diameter, ζ-potential, and molecular weight

The mean hydrodynamic diameter (D_h) and size distribution of the nanogels were measured using dynamic light scattering on a Nano ZS series (Malvern Instruments, UK) Zetasizer equipped with a 4 mW helium/neon laser at a wavelength output of 633 nm and backscattering was measured at a detection angle of 173°. On the other hand, ζ-potential was calculated from the electrophoretic mobility of the nanogels in a mini-electrophoretic DTS-1070 capillary cell (Malvern Instruments, UK). During the measurements, the samples were

diluted 10-times with 10 mM phosphate buffer (pH 7.4) for analysis at 25 °C. Each value was measured at least six times.

The same instrument was used for estimation of molecular weight using a static light scattering method as described elsewhere for crosslinked polymers [33]. Briefly, samples were prepared in 90 % DMSO (vol. %) and then adjusted with 10 mM phosphate buffer (pH 7.4) to 0.25 - 1 mg mL^{-1} concentrations and allowed to completely hydrate for 24 h. The final DMSO concentration in samples was DMSO: buffer (1:10, vol. %). Molecular weight was estimated from the intercept at zero concentration from Debye-plots, where the time-averaged intensity of scattering (therefore, static) for the samples against the single angle was compared to the time-averaged scattered light from a standard sample of toluene, latter was used as a reference.

2.4.2. Far-UV Circular dichroism (CD)

The CD spectra (180 - 260 nm) were measured on a Chirascan Plus (Applied Photophysics, UK) spectropolarimeter using a 1.0 mm path length quartz cuvette at 25 °C. The content of the α-helix, β-sheet, and random coil structures in the protein moiety of the nanogels was calculated on the DICHROWEB server using the K2D method [34]. During the measurements, the samples were diluted 10-times with 10 mM phosphate buffer (pH 7.4) for analysis at 25 °C.

2.4.3. Wide-angle X-ray diffraction (XRD)

The XRD diffractograms of lyophilized nanogels were recorded at 25 °C, over an angular range, $2\theta°$ = 5 - 25°. The sample was mounted on an aluminum sample holder and leveled with a glass slide for examination on a D8 Focus (Bruker AXS, Germany) X-ray diffractometer using Cu Kα (λ = 0.154 nm) radiation.

2.4.4. Electron microscopy

Transmission electron micrographs (TEM) were obtained on a Tecnai G2 F20 S-TWIN (FEI Company, USA) electron microscope. The nanogels were diluted 10-times with 10 mM phosphate buffer (pH 7.4), deposited over a carbon-coated copper grid, and then air-dried before imaging at an accelerating voltage of 20 kV.

Scanning electron micrographs (SEM) were obtained on a JSM 6390 LV (JEOL, Singapore) electron microscope. Lyophilized nanogels were sputter-coated with gold over the sample stage before imaging at an accelerating voltage of 20 kV.

2.4.5. Thermogravimetric analysis (TGA)

TGA was performed on a TG 209 F1 Libra (NETZSCH, Germany) thermogravimetric analyzer. For TGA measurements, the mass of lyophilized nanogels was monitored under nitrogen (20 mL min^{-1}) at temperatures from 20 - 700 °C at a rate of 10 °C min^{-1}.

The first derivative of the mass % in TGA thermograms were plotted (*i.e.* the derivative thermogravimetric (DTG) thermograms) as described elsewhere [35]. The degradation temperature (T_d) of the protein or polysaccharide components of the nanogels was estimated from the temperature corresponding to the maximum mass % change in DTG thermograms. Based on known values of T_d, the mass loss (m_1) in either protein or polysaccharide components and the total mass loss in the nanogels (m_2) were utilized to calculate the thickness of the core and shell as, $\left(\frac{m_1}{m_2}\right) r_h$, where r_h is the radius of the nanogels *i.e.* $\frac{D_h}{2}$ obtained from the dynamic light scattering results..

2.5. *In vitro* oral-gastrointestinal digestion of nanogels

In vitro digestion was carried out using a method described earlier by Minekus et al. [36] with some modifications. Briefly, 100 mg of nanogels were used for each experiment and mixed with salivary α-amylase (75 U mL^{-1}) and $CaCl_2$ (0.75 mM) solution for 5 min at 37 °C to

replicate oral phase digestion. This was followed by the addition of the simulated gastric fluid containing 0.26 g L^{-1} KCl, 0.06 g L^{-1} KH_2PO_4, 1.05 g L^{-1} $NaHCO_3$, 1.38 g L^{-1}NaCl, 0.12 g L^{-1} $MgCl_2(H_2O)_6$, 0.02 g L^{-1} $(NH_4)_2CO_3$ and 1.02 - 1.40 × 10^4 U mL^{-1} pepsin, pH of the solution was adjusted to 2.20 ± 0.05. The simulated gastric digestion was carried out for 30 min. Intestinal digestion was initiated by adding simulated intestinal fluid containing 0.25 g L^{-1} KCl, 0.05 g L^{-1} KH_2PO_4, 3.57 g L^{-1} $NaHCO_3$, 1.12 g L^{-1} NaCl, 0.33 g L^{-1} $MgCl_2(H_2O)_6$, 0.44 g L^{-1} $CaCl_2.2H_2O$, 0.23 g L^{-1} bile salts, and 0.12 g mL^{-1} pancreatin (lipase activity: > 8 U mg^{-1}, amylase activity: > 100 U mg^{-1}, protease activity: > 100 U mg^{-1}). The pH of the solution was adjusted to 6.80 ± 0.05. The simulated intestinal digestion was carried out for 265 min, allowing the total oral-gastrointestinal digestion to be 300 min. The pH was maintained during the entire digestion process by the addition of HCl and NaOH, as necessary.

The digesta was diluted using SDS-PAGE loading buffer and subjected to SDS-PAGE analysis as described earlier [31], at a protein load of 10 μg $well^{-1}$. Relative intensities in SDS-PAGE gels were measured using the open source code ImageJ (NIH, USA).

2.6. *In vitro* cellular internalization of nanogels into cancer cells and cell viability

The HT29 and A549 cells (diseased and control cellular models, respectively) were maintained in complete DMEM medium supplemented with 10 wt. % FBS and penicillin/streptomycin. The confluent cells were seeded into 6-well plates (ca. 0.5 × 10^6 - 0.75 × 10^6 cells $well^{-1}$). For evaluating cellular internalization, FITC was used owing to its narrow emission maximum at 525 nm compared to the broad emission of curcumin in aqueous environments [37]. Briefly, 5 μg ml^{-1} nanogels were tagged with 1.28 μM FITC mg^{-1}, *via* the method of encapsulating curcumin as described in section 2.3. The nanogels were further stirred in the dark for 12 h at room temperature. The excess FITC was removed using ultracentrifugation in Amicon® filters (10-washes). The nanogels were designated as

299 BSM_{FITC}. Appropriate controls without folic acid or any conjugation with ACS (BAM and
300 BSA nanogels) were tagged similarly with FITC and denoted as BAM_{FITC} and BSA_{FITC},
301 respectively. The FITC-tagged nanogels (5 μg ml^{-1}) were added to the cells in 1 wt. % FBS
302 containing medium for 24 h at 37 °C. After treatment, the cells were washed and incubated
303 with phalloidin tagged with Alexa Fluor 568 in the dark (60 min at room temperature) to stain
304 the F-actin filaments of the cells. The cells were then mounted with ProLong Gold Antifade
305 mounting solution with DAPI to stain the cell nuclei and imaged using an IX83 (Olympus,
306 Japan) fluorescence microscope. Relative intensities in micrographs were measured using
307 ImageJ (NIH, USA).

308 An acridine orange/ethidium bromide (AO/EB) assay was used for the identification
309 of apoptosis as described earlier [38]. Briefly, cells were seeded in 6 well tissue culture plates
310 (0.5×10^6 cells $well^{-1}$) and treated with free curcumin or the curcumin encapsulated nanogels
311 for 24 h at 37 °C. After removal of medium, cells were washed and then stained with AO
312 (50 mg mL^{-1}) and EB (5 mg mL^{-1}), respectively for 5 min at room temperature and examined
313 under a fluorescence microscope. Apoptosis + necrosis in micrographs were measured using
314 ImageJ (NIH, USA) based on the intensity of EB entry into the nonviable cells (dye entry
315 follows, early apoptotic < late apoptotic < necrotic cells) and emission of red fluorescence by
316 intercalation into DNA [38].

317 An MTT-based colorimetric assay was performed to examine the *in vitro* cellular
318 cytotoxicity. Cells were seeded (7.5×10^3 cells $well^{-1}$) in a 96-well plate and incubated
319 overnight at 37 °C. Next, the cells were treated with free curcumin or the nanogels (1, 5, and
320 10 μg mL^{-1}) in 1 wt. % FBS containing medium for another 24 h at 37 ºC. Following the
321 treatment, cells were washed with DPBS, and MTT (5 mg mL^{-1}) was added for 4 h at 37 °C.
322 The medium was discarded and 150 μL of MTT-dissolving solution (0.1 % TERGITOL™
323 Type NP-40 and 4 mM HCl in isopropanol) was added to each well and agitated in an orbital

shaker for 15 min. Formazan absorbance was measured at 590 nm. Absorbance values were corrected against the absorbance of cells without any treatment (control).

Note, penicillin/streptomycin was not used in the AO/EB and MTT assays to limit any antibiotic-induced interference in cell viability.

2.7. Statistical analysis

Analysis of variance (ANOVA) and Tukey's HSD Post Hoc analyzes were conducted using SPSS 8.0 (SPSS, Inc., USA). Treatment means were considered significantly different at $p < 0.05$.

3. Results and discussion

3.1. Synthesis and characteristics of the albumin (BSA)-folic acid functionalized amylopectin (SF20) copolymer conjugates

The folic acid functionalized amylopectin (SF20) and amylopectin (ACS, control) was conjugated to bovine serum albumin (BSA_{native}) *via* a Maillard reaction, under water-restricted conditions. This yielded the BSM_{con} and BAM_{con} copolymer conjugates. For both the conjugates *i.e.* with or without functionalization with folic acid groups, the increasing degree of glycation was dependent on the reaction time (corresponding to 6, 12, 24, and 48 h) as evidenced in Figure 1 derived from Figure S1a. The SDS-PAGE electrogram confirming the formation of conjugates as evidenced by high molecular weight glycoprotein smears in BSM_{con} and BAM_{con} as shown in Figure S1a. The BSA_{native} protein (L 2 in Figure S1a) was prominent at ca. 66 kDa, which is consistent with the theoretical molar mass [31]. From a closer examination of Figure 1, it appears that SF20 is more potent in conjugating to the protein, in comparison to ACS. Additionally, the *O*-phthaldialdehyde assay (evaluated for lysine) sheds further light into this covalent binding behavior. For BSM_{con} and BAM_{con}, 41.20 ± 2.77 and 27.54 ± 1.15 % lysine residues in the protein were conjugated to SF20 and ACS,

348 respectively (data not shown). We postulate that the negatively-charged SF20 (ca. -24 mV
349 [22]) was favored in terms of the spatial proximity to a greater number of cationic lysine
350 residues housed in the protein at pH 8.0. This electrostatically attractive contribution may
351 have facilitated the Maillard reaction to a greater extent as shown in Figure 1, which in the
352 case of weakly-anionic ACS (ca. -3 mV [22]) was marginal.

353 Noteworthy that extending the Maillard reaction time (> 24 h) resulted in water-
354 insoluble products (the plateauing region in Figure 1). Similar observations have been made
355 earlier, where the solubility of albumin-alginate Maillard reaction conjugates suffered when
356 subjected to a prolonged Maillard reaction time [39].

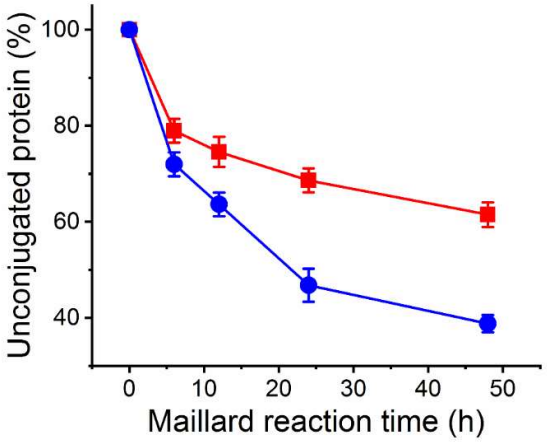

357

358 Figure 1. Unconjugated protein (%) at different Maillard reaction times; BSM_{con} (blue, ●) and
359 BAM_{con} (red, ■). Error bars represent standard deviations of independent image analyses
360 ($n = 10$).

361

362 We used FT-IR to comprehend the short-range molecular order of the conjugates. The
363 spectra (Figure 2) evidenced the characteristic peaks around 2852 cm^{-1}. The peak attributes to
364 the NH-group of pterin ring in folic acid [22] confirming the functionalization by folic acid
365 ligands in the case of BSM_{con}. This characteristic peak was absent in both BAM_{con} and
366 BSA_{native}. The FTIR spectra of BSM_{con} and BAM_{con} in comparison to BSA_{native}, evidenced a

ca. 65 and 22 % reduction in the intensity of the band around 2930 cm^{-1} (obtained from peak area analysis). This may be assigned to intramolecular hydroxyl and amino group H-bonding amidst the amino acid residues residing in the protein [40], which upon conjugation appears to be de-bonded, resulting in the unfolding of the polypeptide structure. A weakening of the absorbance signal around 1656 cm^{-1} was additionally evidenced. The peak corresponds to the amide I region (Figure 2, inset) of the protein, comprising C=O stretching and C-N bending. Also, a dampened absorbance around 1539 cm^{-1} was observed, which may be attributed to the unfolding of the amide II region (Figure 2, inset) of the protein, comprising N-H bending and C-N stretching. Both indicate that a protein structure unfolding occurred *via* conjugation with SF20/ACS. A similar unfolding of protein structure has been witnessed earlier during the Maillard reactions of albumin with glucose and mannose [41]. Interestingly, protein structure unfolding was more pronounced in the case of SF20, in comparison to ACS (Figure 2, inset). This appears to have had implications in the promotion of Maillard conjugation of the former, as evidenced during SDS-PAGE and OPA analysis.

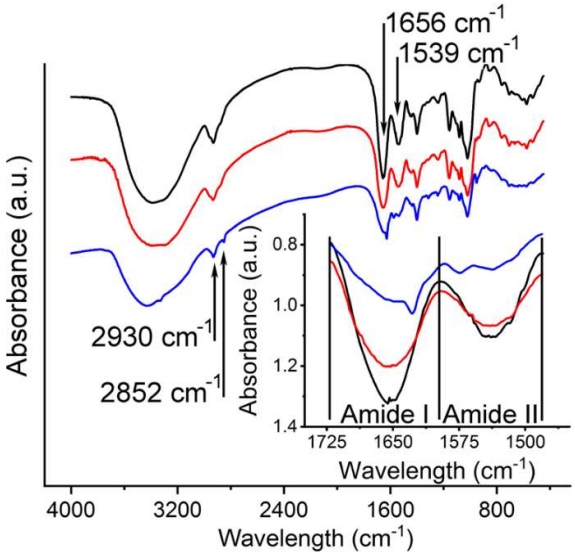

Figure 2. FTIR spectra of BSA_{native} (black), BAM_{con} (red), and BSM_{con} (blue). Arrows indicate characteristic peaks. The spectra are offset vertically for clarity. Inset shows the Amide I and II regions of the spectra.

Additionally, Figure S1b, left, indicated that the conjugates exhibited pronounced amphiphilicity evidenced from the formation of the film at the *n*-hexane/phosphate buffer interface even after strenuous shaking. The schematic illustration of this amphiphile assembly at the oil/water interface is depicted in Figure S1b, right, and corroborates with findings of previous protein-polysaccharide studies [17, 42].

3.2. Mean hydrodynamic diameter and ζ-potential of the nanogels

The synthesized conjugates were subjected to thermal gelation to fabricate nanogels. The mean hydrodynamic diameter (D_h) of the BSM (89.50 ± 10.88 nm; PDI, 0.24) and the control BAM (105.58 ± 11.24; PDI, 0.28) nanogels were observed to be significantly smaller ($p < 0.05$) than their protein alone counterpart, BSA (232.73 ± 31.24; PDI, 0.41). It seemed that the conjugation of polysaccharide (SF20/ACS) to protein prevented the formation of larger heterogeneous nanogels. A polysaccharide surface coverage of protein nanogels is known to provide a steric barrier for stability against aggregation [17, 19]. This was reinstated by the narrow distribution of BSM and BAM, in comparison to the bimodal distribution for the BSA nanogels (Figure 3a).

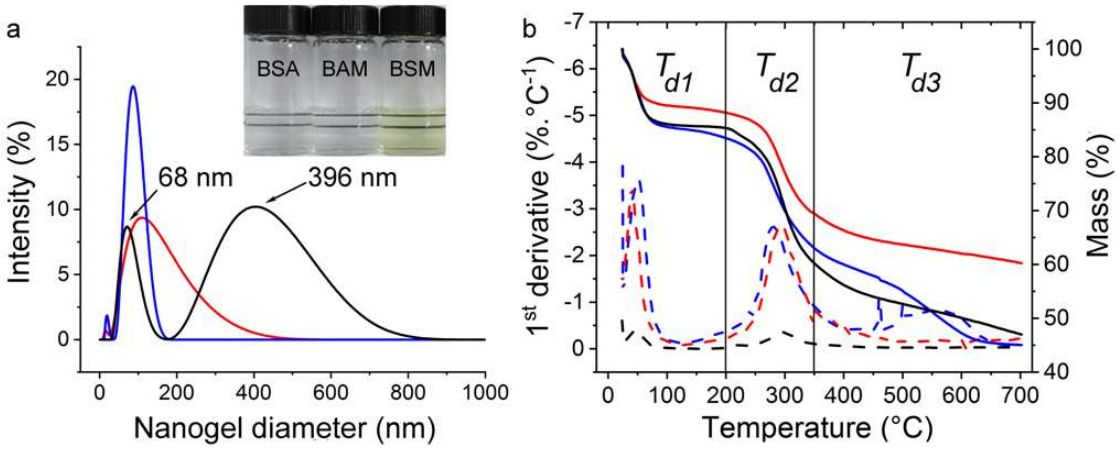

Figure 3. Size distribution of BSM (blue), BAM (red), and BSA (black) nanogels. Inset shows the nanogel solutions. Double black lines behind solutions vials are present to help visualize solution turbidity (a). Solid lines and dashed lines (BSM (blue), BAM (red), and BSA (black)

405 nanogels) represent TGA and DTG thermograms, respectively. Solid vertical lines indicate
406 mass loss intervals. T_d represents the degradation temperature (b).
407

408 Additionally, the ζ-potential of BSM nanogels was -24.40 ± 0.43 mV, significantly (p
409 < 0.05) higher in comparison to -8.76 ± 0.24 and -18.60 ± 0.45 mV for the BAM and BSA
410 counterparts at pH 7.4, respectively. The ζ-potential of SF20 and ACS are known to be -24.50
411 ± 6.41 and -3.95 ± 0.32 mV, respectively [22]. This further confirms an effective surface
412 coverage of the proteinaceous core by SF20 and ACS polysaccharide shell. The higher net ζ-
413 potential value of BSM suggests the forming of a stable colloidal dispersion against protein
414 aggregation during nanogel formation.

415 **3.3. Structural characteristics of the nanogels**

416 The synthesized protein-polysaccharide conjugates that thermally-crosslink to produce the
417 core-shell nanogels, comprised of a protein tail and a polysaccharide head, as depicted in
418 Figure 4a (left). In the conjugate, the D_h of a single monodisperse BSA_{native} protein
419 comprising the tail is ca. 5 - 6 nm (the theoretical assumption that the radius of the protein is
420 $0.066M^{\frac{1}{3}}$, where M is the protein mass in Daltons [43]) and the D_h of SF20 comprising the
421 head is ca. 300 nm [22]. Therefore, the tail is orders of magnitude smaller than the head,
422 allowing the conjugates to reflect as cone-shaped macromolecules (Figure 4a, left). Such cone
423 shaped amphiphiles favor a positive mean curvature (surfaces moving away from the normal)
424 during assembly *via* thermal-crosslinking, forming Type I or oil-in-water-like architectures
425 [44], as depicted in Figure 4a, right. The impetus for this assembly should be derived from the
426 amphiphilic necessity of, a) the hydrophilic polysaccharide head to be particularly hydrated at
427 the water interface, and b) the hydrophobic denatured protein tail sequestered to the interior to
428 reduce oil-water interactions. The dynamic light scattering data and ζ-potential of the BSM
429 and BAM in comparison to BSA nanogels agree with this proteinaceous core and

polysaccharide shell-type structure, which is in agreement with previous studies [9, 18, 45]. The schematic structures of these core-shell nanogels are shown in Figure 4b-d.

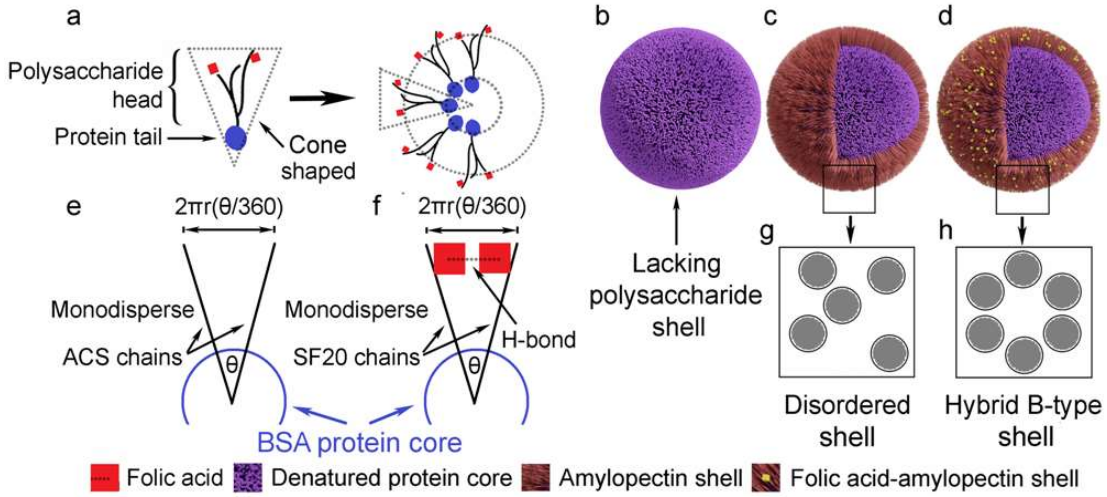

Figure 4. Schematic illustrations of the dimension of copolymer conjugates and core-shell nanogel architecture (a), BSA (b), BAM (c), and BSM (d) nanogels (nanogels were prepared and rendered using the open source code Blender 2.8, https://www.blender.org). Arc length distance and curvature effects of BAM (e) and BSM (f) nanogels. The structural arrangement of polysaccharide polymer chains in the BAM (g) and BSM (h) shell. Schematic illustrations are not drawn to scale.

The thickness of the core and shell of the nanogels were estimated roughly from the protein and polysaccharide mass composition of the nanogels evaluated from DTG thermograms (derived from the derivative of TGA thermograms) (Figure 3b). In the three-stage thermal degradation profile, the first (T_{d1}) corresponds to the evaporation of water molecules [46] and therefore was not assumed to arise from the nanogels. The second (T_{d2}) and third (T_{d3}) thermal degradation profile is assumed to arise from the protein and polysaccharide parts of the nanogels, respectively. TGA and DTG thermograms of ACS and SF20 are shown in Supplementary Figure S1d for comparison. We evidenced ca. 54 nm core diameter (*i.e.* radius of core, r_{core} is ca. 27 nm) with an 18 nm thick shell for BSM and ca. 67 nm core diameter (*i.e.* radius of core, r_{core} is ca. 34 nm) with a 19 nm thick shell for BAM. Note, the density difference of BSM and BAM nanogels were insignificant ($p > 0.05$) at 1.01

± 0.29 and 1.48 ± 0.22 g cm^{-3}, respectively as estimated using a PYC-100A (Porous Material Inc., USA) He-pycnometer (density should be considered with precaution as the error rate was ≥ 0.2 g cm^{-3}). Since the D_h of a monodisperse BSA_{native} protein is ca. 5 - 6 nm as discussed earlier, the number of unit proteins within the core of BSM and BAM nanogels can be estimated as ca. 95 and 180, respectively from $\frac{Volume_{core}}{Volume_{BSA_{native}}} \times 0.74$ [47] (considering unit proteins being equal-sized spheres, their closest packing density is, $\frac{\pi}{\sqrt[3]{2}} \approx 0.74$; *i.e.* 74 % of the volume). This further ascertains that the greater net negative charge of BSM_{con} restricted the excessive aggregation of protein in BSM nanogels during formation, in comparison to BAM_{con}.

The structural characteristics of the proteinaceous core of the nanogels were explored using far-UV circular dichroism. Circular dichroism revealed that BSA_{native} comprised of a ca. 71 % α-helical structure, which is in close agreement with published data [48]. However, all the nanogels demonstrated a significant loss of the α-helical structure, alongside an increase in the quantity of random coil structure and formation of β-sheets, as evidenced in Table 1 derived from Figure S1c. Denaturation of BSA at 80 °C seems to have resulted in the complete unfolding of the BSA polypeptide structure *via* heat-induced gelation [49, 50], which upon cooling allowed BSA to (re)fold into nanogel conformation, in agreement with an earlier work [51].

Table 1. Structural aspects of the proteinaceous core.

	α-helix	**β-sheets**	**Random coil**
		%	
BSA_{native}	71	3	26
BSM	23	21	56
BAM	23	22	55
BSA	24	21	55

$BSA_{native,}$ native bovine serum albumin used without any treatment; BSM, bovine serum albumin + folic acid functionalized amylopectin (SF20) conjugate nanogels; BAM, bovine serum albumin + amylopectin (ACS) conjugate nanogels without added folic acid (control); and BSA, Bovine serum albumin nanogels without any conjugation (control).

The TGA thermograms were further utilized to estimate the packing density of the polysaccharide chains in the SF20/ACS shell masking the molten proteinaceous core [52]:

$$\sigma_{TGA} = \frac{\frac{M\,\%_{Shell}}{M\,\%_{core}}\rho_{core}\frac{4}{3}\pi r_{core}{}^{3}N_A}{MW4\pi r_{core}{}^{2}} \quad \text{Eq. (3)}$$

where M $\%_{shell}$ and M $\%_{core}$ are the mass of SF20/ACS and BSA derived from Figure 3b. The M $\%_{shell}$ was divided by the polymer mass per chain (*i.e.* polymer molecular weight determined for SF20 and ACS polymers subjected to temperature-sheared conditions of nanogel preparation (see preparation method in section 2.3) using static light scattering were 6.47×10^5 and 2.84×10^6 Da, respectively over Avogadro's number) to estimate the number of polymer units in the sample. Note, the molecular weight of native SF20 and ACS were 2.04×10^7 and 1.82×10^7 Da, respectively; where ACS values are in agreement with previous reports [26, 53]. It appears that the polymer molecular weight was susceptible to shear and temperature induced degradation plausibly causing chain breakage at the polysaccharide branching points [54]. This was greater for SF20 as compared to ACS, in agreement with a previous report for citric acid functionalized starch with 75 % amylopectin [55]. The denominator in Eq. (3) represented the total surface area of the nanogel cores in the sample *i.e.*, the surface area per unit nanogel core ($4\pi r_{core}{}^{2}$) multiplied by the total number of nanogel cores. The total number of nanogel cores was estimated from the M $\%_{core}$ divided by mass of a unit nanogel core, which correlates with the density of BSA core (assumed from BSA nanogel density *i.e.* ρ_{core} = ca. 1.48 g cm^{-3}) multiplied by the volume of a unit nanogel core ($\frac{4}{3}\pi r_{core}{}^{3}$). And the volume and surface area calculations assumed that the nanogels

were spherical, in congruence with TEM images, which are discussed later in Section 3.5. From Eq. (3), we estimated the packing density of SF20 and ACS polysaccharide chains in the shell per nm^2 of the proteinaceous core to be 8.15×10^{-3} and 2.00×10^{-3}, respectively. The number of SF20 and ACS chains attached to each nanogel core was estimated from the packing density (σ_{TGA}) and the radius of the nanogel core (r_{core}) as, $\sigma_{TGA} 4\pi {r_{core}}^2$ [56] and the calculated value for SF20 and ACS was 75 and 28, respectively. Note, each chain is a hyperbranched polysaccharide with a tree-like topology. The packing order within this polysaccharide shell appeared to be an A-, B- (depicted in Figure 4h), and V-type polymorphism for the BSM nanogels, whereas, a mostly disordered packing (depicted in Figure 4g) was apparent for the BAM nanogels except for a single A-type peak, as analyzed by XRD (Figure S2a, b). BSA nanogels exhibited a characteristic scattering at *2θ*, ca. 5°, which was observed in all the nanogels. This confirms that the diffraction contributions other than *2θ*, 5° in BSM and BAM should only arise from the liquid-crystalline state of the polysaccharide gelators in the shell. In BSM, the B- and V-type liquid crystalline contributions are a larger hybrid hexagonal packing known to be driven by the self-assembly of SF20 chains [22, 25] and single-left handed helical packing in the presence of guest molecules [57] such as folic acid in this case, respectively. The presence of inter-lamellar water, confirmed by our TGA experiments, is essential to such liquid crystalline contributions, as demonstrated earlier [22]. Additionally, it appears that the large curvature effect produced by the relatively small sizes of the nanogels, do not favor self-assembly of the ACS chains in BAM nanogels, leading to the observed disorder in the shell. Note, the inter-chain arc length distance between two monodisperse chains originating from the curved surface of the core at *θ*° will increase at the rate of $4\pi D \left(\frac{\theta}{360}\right)$, as *D i.e.* chain length increases. The increased inter-chain distance makes their self-assembly energetically unsustainable. Yet, the substituted folic acid on SF20 chains acts as bridges and surmounts the distance barrier for

self-assembly of the BSM shell to occur. This phenomenon is depicted in Figure 4e, f. Further evaluation of these core-shell nanogels using small-angle neutron scattering with contrast variation might provide detailed information on these thermally-crosslinked nanogels, which is beyond the scope of this work.

3.4. *In vitro* oral-gastrointestinal digestion of the nanogels

Since the BSM nanogels comprised of a liquid crystalline polysaccharide shell, we hypothesized the shell to modulate the oral-gastrointestinal digestion behavior of the embedded protein core. Additionally, this was of applicative importance to delivery *via* the oral route, considering the physiological degradation of oral-gastrointestinal transit. Figure 5 shows the SDS-PAGE electrogram of the digesta of BSM, BAM (control), and BSA (control) nanogels. After 300 min of simulated *in vitro* digestion, ca. 35 % of BSM remained intact in comparison to ca. < 5 % of both BAM and BSM (measured *via* image analysis, see Figure S3a). This is evidenced by the prominent band at ca. 66 kDa alongside glycoprotein smears at higher molecular weights. Besides the high molecular weight smears, it seems that the protein (ca. 66 kDa band) was also mildly glycated, thus evidencing hindered digestion.

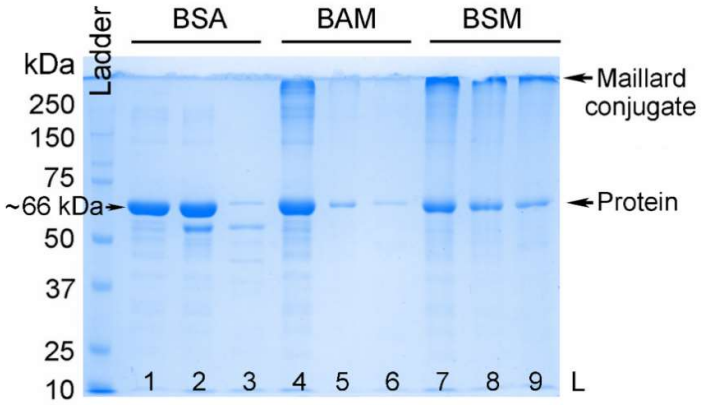

Figure 5. SDS-PAGE electrogram of *in vitro* oral-gastrointestinal digesta. Lanes L 1: BSA, 0 min (sample, oral-gastrointestinal digestion time), L 2: BSA, 30 min; L 3: BSA, 300 min, L 4: BAM, 0 min, L 5: BAM, 30 min, L 6: BAM, 300 min, L 7: BSM, 0 min, L 8: BSM, 30 min, L 9: BSM, 300 min.

One can argue that the Maillard reaction-based conjugation *via* covalent binding of the carbohydrate moiety to the polypeptide backbone altered the conformation of the latter, thereby limiting enzymatic accessibility through steric hindrance [49]. Ideally, this should have helped to limit the digestion in both BSM and BAM nanogels; however, it was not the case. BSM appears to be resilient in evading digestion in the larger scheme of 300 min of digestion. We believe that the SF20 shell of BSM nanogels to exert this restrictive phenomenon on digestion, owing to the B- and V-type liquid crystalline packing [25]. This shell-packing resisted the initial digestion by amylases and provided a steric safeguard to the protein core from *in vitro* digestion by proteolytic enzymes. We propose that the structural aspects of polysaccharide chain packing in the shell relate closely to protection against physiological digestion.

3.5. Effect of curcumin encapsulation on the colloidal structure of nanogels

The core-shell structure was further evaluated for structural effects upon encapsulation of the model therapeutic hydrophobe, curcumin. The latter profoundly altered the D_h of the nanogels as the curcumin load was incremented from 0.02 to 0.2 mg mL^{-1}. The BSM_{cur} nanogels exhibited 100 % curcumin encapsulation efficiency (*CEE*), encapsulating all the curcumin molecules until a curcumin load of 0.05 mg mL^{-1} (Figure S3b). In spite of the poor solubility of curcumin in water, BSM_{cur} leads to the formation of a clear yellow dispersion (Figure 6, inset). Beyond this level of loading, *CEE* decreased. The D_h of the BSM_{cur} was observed to remain fairly consistent (ca. 90 nm) until a curcumin load of 0.1 mg mL^{-1} (Figure 6). However, a significant ($p < 0.05$) increase in D_h to 345.70 ± 25.21 nm (PDI, 0.38) was observed at 0.2 mg mL^{-1} curcumin load (Figure 6). For the control experiments, an increase in D_h was observed for the BAM_{cur} and BSA_{cur} nanogels at 0.2 mg mL^{-1} curcumin load with high polydispersity (D_h, 1488.71 ± 49.21; PDI, 1.0 and 2380.34 ± 115.21 nm; PDI, 0.51, respectively, Figure 6). This was significantly higher ($p < 0.05$) when compared to the

566 BSM_{cur}. Beyond > 0.2 mg mL^{-1} curcumin load, all nanogels displayed heavy precipitation and

567 reliable measurements could not be performed.

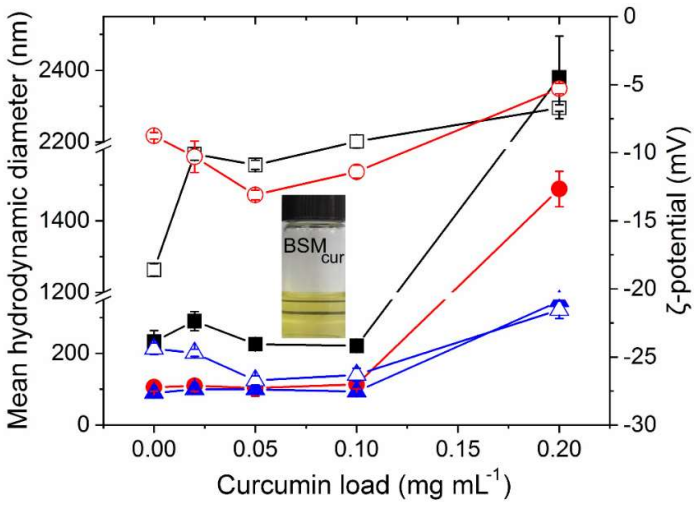

568

569 Figure 6. Mean values of hydrodynamic diameter (solid symbols) and ζ-potential (open
570 symbols) of BSM (blue, ▲, △), BAM (red, ●, ○), and BSA (black, ■, □) nanogels. Error bars
571 represent standard deviation from independent measurements, $n = 6$. Inset shows clear-yellow
572 dispersion of BSM_{cur} nanogels, 0.05 mg mL^{-1} curcumin load. Double black lines behind
573 solution vial are present in order to help visualize solution turbidity. CEE and CLE % of
574 nanogels against curcumin load are shown in Figure S3b.

575

576 Transmission electron micrographs evidenced spherical BSM_{cur} core-shell nanogels
577 (curcumin load, 0.05 mg mL^{-1}, Figure 7a). Here, the dense shell (dark grey layer, Figure 7a
578 enlarged inset) encompassing the core (light grey) appears to originate from the diffraction
579 contrast of the ordered liquid crystalline signature of SF20, as observed in XRD results
580 (Section 3.3) and earlier small and wide-angle X-ray scattering [22, 25]. Note, the shell
581 thickness (Figure 7a, enlarged inset) is in close agreement with the theoretical estimates from
582 TGA in Section 3.3. Additionally, BSM_{cur} nanogels with 0.2 mg mL^{-1} curcumin load appeared
583 enlarged in congruence with the dynamic light scattering results and evidenced a much thicker
584 shell (Figure 7b, enlarged inset).

585 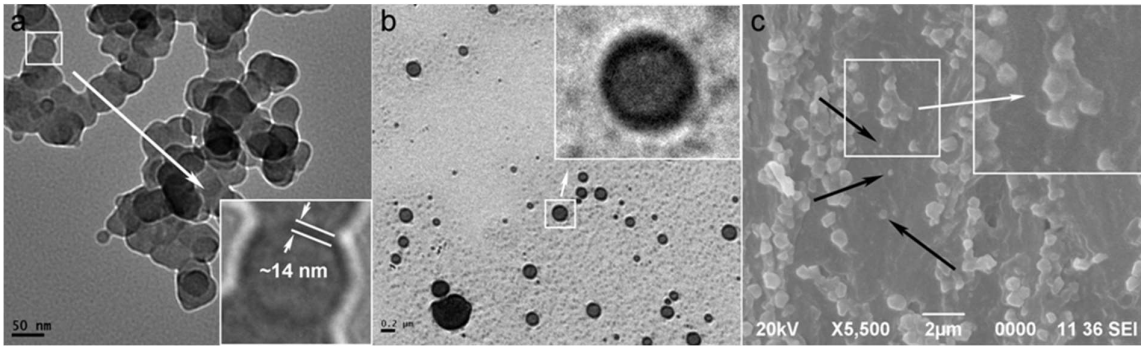

586 Figure 7. Transmission electron micrographs (TEM) of BSM_{cur}, curcumin load, 0.05 mg mL^{-1},
587 scale bar is 50 nm (a) and 0.2 mg mL^{-1}, scale bar is 0.2 µm (b). Scanning electron micrograph
588 (SEM) of BSM_{cur} (curcumin load, 0.2 mg mL^{-1}), scale bar is 2 µm (c). Insets represent
589 zoomed images.

590

591 It has been previously reported that curcumin encapsulation dramatically alters the
592 structural characteristics such as the D_h of particles [31, 51]. A bound hydrophobic molecule
593 may act as connective bridges between spatially adjacent inter-particle proteins *via* H-bonding
594 [14, 52]. Additionally, a recent study by Wong et al. [53] suggested that carbohydrates can be
595 involved in hydrogen bonding with curcumin, promoting their self-assembly *via* non-covalent
596 forces. We postulate that in our case, incrementing the curcumin load (notably > 0.1 mg mL^{-1})
597 promoted non-covalent interactions amidst the protein-polysaccharide chains of conjugates in
598 the pre-particle solution that was undergoing thermal gelation, leading to aggregation, and
599 consequently increase in D_h of the resulting nanogels. This aggregation was additionally
600 observed in scanning electron micrographs showing BSM_{cur} nanogels (marked by black
601 arrows, Figure 7c) forming clustered-superstructures that appear to be fused (Figure 7c, white
602 enclosure and enlarged inset to the right), in agreement with previous reports [28, 54].
603 However, the SEM image should be considered with precaution, as the observations might
604 have been influenced by the dehydration steps during the sample preparation process for
605 microscopy.

Additionally, a systematic increase in the corresponding ζ-potential of BSM_{cur} nanogels (-24.40 ± 0.43 to -26.72 ± 0.34 mV) was observed upon increasing the curcumin load to 0.05 mg mL^{-1} (Figure 6). Note, at curcumin load of 0.1 mg mL^{-1} (> 0.05 mg mL^{-1}) the ζ-potential (-26.31 ± 0.48 mV) was not significantly ($p > 0.05$) different to the former, indicating a plateau. Beyond this, the ζ-potential decreased significantly ($p < 0.05$) to -21.54 ± 0.64 mV (curcumin load, 0.2 mg mL^{-1}). For the controls, BAM_{cur} and BSA_{cur} (curcumin load, 0.2 mg mL^{-1}), the ζ-potential value were observed to be significantly ($p < 0.05$) lower (-5.29 ± 0.38 and -6.72 ± 0.24 mV, respectively) in comparison to the BSM_{cur} counterparts. Such low values, ca. -5 mV is expected to cause aggregation [58-60] as observed in their increased D_h. It is noteworthy, that both BSM_{cur} and BAM_{cur} nanogels demonstrated alike magnitudes of ζ-potential and *CLE* % (cp. Figure 6 and Figure S3b). We measured the ζ-potential of curcumin to be -4.34 ± 0.34 mV (non-ionic Tween 20 was used to create the interfacial phenomenon at pH 7.4), in agreement with an earlier report [7]. It appears that the mass % of the nanogels comprising the encapsulated curcumin contributes to the overall charge of the nanogels and can profoundly alter it, as also observed in a previous study [61].

The curcumin-loaded nanogels were further evaluated for stability in physiological conditions. SDS-PAGE results for the BSM_{cur}, BAM_{cur}, and BSA_{cur} at 0.05 mg mL^{-1} curcumin load, displayed equivalent resistance to digestion as compared to the empty nanogels (cp. Figure 5 and Figure S4a). Previous *in vitro* digestion models studies have demonstrated that curcumin degradation is unlikely to occur during simulated gastric digestion *i.e.* acidic pH owing to curcumin adopting the stable keto-form in such environments, which is contrary to the rapid degradation of curcumin in simulated intestinal digestion conditions *i.e.* near neutral pH and under visible light [4, 28, 62]. Therefore, a photo-degradation study of the encapsulated curcumin at neutral pH was carried out as it is relevant for further application of the nanogels in formulations. Figure S4b demonstrates the time-dependent 50 % degradation

631 of free curcumin to occur within ca. 140 min at physiological pH under direct light at 25 °C
632 (absorbance, 420 nm). However, all nanogels exhibited ca. < 50 % curcumin degradation up
633 to 900 min in the same conditions. Any curcumin degradation observed in the encapsulated
634 form is likely to stem from weakly bound curcumin molecules to the nanogels [63]. We
635 believe that the nanogels enabled the increased resilience to degradation *via* the encapsulation
636 of curcumin within hydrophobic pockets of the proteinaceous core that was isolated from the
637 bulk physiological environment. XRD results were in agreement. Free curcumin exhibited
638 sharp peaks at 2θ°, 12°, 15°, 17°, 18°, 21°, and 24°, implying a highly crystalline curcumin
639 form I structure (Figure S5a). This is typical for commercial curcumin [64]. Such
640 characteristics were absent in the curcumin-loaded nanogels (other than diffractions at 2θ°,
641 18° and 21°) indicating that the hydrophobe was fully solubilized within the proteinaceous
642 core of the nanogels and was unable to re-crystallize within the nanoscale confinement
643 (Figure S5b).

644 Further monitoring of curcumin release kinetics from the nanogels and degradation
645 under physiological stress (pH, temperature, and oral-gastrointestinal digestion) may be
646 interesting to establish a relationship amidst the structural integrity of the nanogels and the
647 persistence of the encapsulated payload.

648 **3.6. *In vitro* cellular internalization and cytotoxicity of nanogels**

649 To assess cellular internalization, a cellular uptake assay was performed in human HT29
650 colon adenocarcinoma cells which overexpress folate receptors. Figure 8a shows BSM_{FITC}
651 nanogels were successfully capable of specifically targeting and internalizing into HT29 cells.
652 The fluorescent green spots around the actin fibers (red) and the cell nuclei (blue) indicate
653 nanogel internalization. We postulate that fluorescent green spots are endosomally engulfed
654 BSM_{FITC} clusters (Figure 8a and inset-right, green globules indicated by yellow arrows).
655 Contrarily, no FITC fluorescence was observed for the BSM_{FITC} nanogels when evaluated on

the folate-receptor negative A549 cells (Figure 8b). Additionally, FITC fluorescence or fluorescent globules were not observed in both the cellular models for the controls, *i.e.* BAM_{FITC} (Figure 8c, d) and BSA_{FITC} (Figure 8e, f), and therefore not investigated hereafter. The internalization of the FITC-tagged nanogels are quantified in Figure 8g and indicates that the SF20 presentation on the shell of BSM_{FITC} drives the observed nanogel internalization, plausibly *via* a folate-receptor dependent internalization mechanism, confirming the specificity.

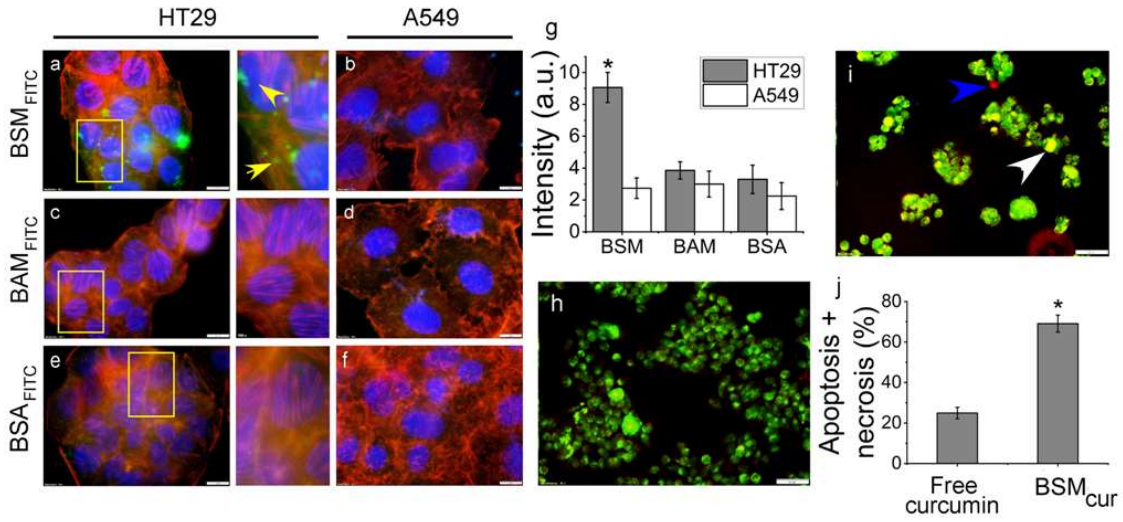

Figure 8. Fluorescence micrographs of folate-receptor positive HT29 and folate-receptor negative A549 cells treated with FITC-tagged nanogels. Yellow zoned regions are enlarged to the right. Arrows (yellow) indicate the internalized of BSM_{FITC} (fluorescent green spots) nanogels. Scale bars are 10 µm (a - f). Control experiments and individual dye emission channels are shown in Figure S6 and S7. Histogram shows quantification of BSM_{FITC}, BAM_{FITC}, and BSA_{FITC} cellular internalization. *$p < 0.05$ (g). AO/EB assay of free curcumin (h) and BSM_{cur} nanogels (i) in HT29 cells. Arrow (blue) indicates necrotic cells and arrow (white) indicate early-stage apoptotic cells. Scale bars are 50 µm. Control experiments and individual dye emission channels are shown in Figure S8. Histogram shows quantification of free curcumin and BSM_{cur} induced early-stage apoptosis (yellow cells) + necrosis (red cells). *$p < 0.05$ (j). Error bars represent standard deviations of independent image analyses, $n = 3$.

Additionally, an AO/EB assay demonstrated that in comparison to equal amounts of free curcumin (Figure 8h), the BSM_{cur} nanogels (5 µg mL^{-1} nanogels with 0.05 mg mL^{-1} curcumin load) after treatment in HT29 cells, evidenced a significant decrease in the

679 proportion of viable cells and increase in the proportion of early-apoptotic + necrotic cells
680 (Figure 8i). Note, bright green chromatin and organized structures indicated viable cells
681 whereas bright green-yellow chromatin and bright red chromatin indicated early apoptotic
682 cells and necrotic cells, respectively [38]. This is quantified in Figure 8j (derived from Figure
683 S8). Apoptosis is a coordinated energy-dependent process that follows a complex cascade of
684 events that link the initiating stimuli to the final demise of the cell [65]. Note, an MTT assay
685 confirmed that free curcumin or BSM nanogels at 1, 5, and 10 μg mL^{-1} exhibited ca. ≥ 80 %
686 cell viability after 24 h of treatment in HT29 cells (Supplementary Figure S9). Therefore,
687 curcumin encapsulated BSM nanogels, *i.e.* BSM_{cur} incremented the retention of curcumin in
688 HT29 cells by 60 % compared to free curcumin in solution and any induction of apoptosis is
689 likely to arise from the increased bioavailability of curcumin in the colon cancer cells.

690 **4. Conclusions**

691 To enable specific targeting of colon cancer cells by folic acid [66], we employed previously
692 reported hyperbranched folic acid functionalized amylopectin (SF20) polymers that
693 demonstrated resilience to oral-gastrointestinal digestion [22, 25] to conjugate with BSA
694 protein (a natural carrier of hydrophobic molecules [9]) *via* Maillard reaction. The resulting
695 sophisticated "cone-shaped" amphiphilic copolymer conjugates were thermally-crosslinked to
696 design unique bovine serum albumin-folic acid functionalized amylopectin (BSM) nanogels
697 with a core-shell conformation such that thermally cross-linked proteinaceous BSM formed
698 the gel-like core and the liquid crystalline (B- and V-type polymorphism) folic-acid
699 functionalized polysaccharide formed the shell. The unique biocompatible core-shell colloidal
700 design demonstrated resistance to *in vitro* oral-gastrointestinal digestion, in addition to
701 specific cellular internalization in the human HT29 colon cancer cells plausibly *via* a folate
702 receptor-dependent internalization mechanism. Encapsulation of curcumin within the BSM
703 nanogels (denoted as BSM_{cur}) allowed solubilization of 0.05 mg mL^{-1} curcumin, which was

ca. two orders of magnitude higher than the reported aqueous solubility (ca. 0.4 - 0.6 μg mL^{-1}) of curcumin at neutral pH [29, 67]. The curcumin encapsulated in BSM_{cur} nanogels demonstrated stability to physiological degradation and effectively induced early-stage apoptosis in HT29 cells, which was not observed for free curcumin in solution. Thus, the present study demonstrates in-depth structural characterization and bio-functional performance of these sophisticated nanogels as delivery vehicles. Insights from this study may provide practical design approaches to tailor-make colloidal core-shell nanogels to increase the oral bioavailability of curcumin or similar hydrophobic drugs for the treatment of colon cancer. Further neutron scattering study is ongoing to clearly understand the structural implications of the shell thickness and ordering of folic acid on cellular internalization of curcumin.

Acknowledgements

PKB is a Commonwealth Scholar funded by the UK government. PKB thanks Netramoni Baruah (Department of Agricultural Engineering, Assam University, India) for technical discussion related to arc length distances. RM acknowledges funding received as a Unit of Excellence (U-Excel) project from the Department of Biotechnology, Government of India [Sanction no. BT/410/NE/U-Excel/2013]. Authors acknowledge the assistance of G Nasir Khan (Faculty of Biological Science, University of Leeds, United Kingdom), Biju Boro (Department of Physics, Tezpur University, India), and, Anil Hazarika and Prakash Kurmi (Sophisticated Analytical Instrumentation Centre, Tezpur University, India) for their technical support in circular dichroism, SEM, and, TEM and XRD, respectively.

References

[1] A.F.L. Rolle, T.K. Chiu, Z. Zeng, J. Shia, M.R. Weiser, P.B. Paty, V.K. Chiu, Oncogenic KRAS activates an embryonic stem cell-like program in human colon cancer initiation, Oncotarget 7(3) (2016) 2159-2174. https://doi.org/10.18632/oncotarget.6818

[2] D. Rosenblum, N. Joshi, W. Tao, J.M. Karp, D. Peer, Progress and challenges towards targeted delivery of cancer therapeutics, Nat. Commun. 9(1) (2018) 1410-1422. https://doi.org/10.1038/s41467-018-03705-y

[3] S. Senapati, A.K. Mahanta, S. Kumar, P. Maiti, Controlled drug delivery vehicles for cancer treatment and their performance, Signal Transduct. Target. Ther. 3(1) (2018) 7-26. https://doi.org/10.1038/s41392-017-0004-3

[4] M. Kharat, D.J. McClements, Recent advances in colloidal delivery systems for nutraceuticals: A case study – Delivery by Design of curcumin, J. Colloid Interface Sci. 557 (2019) 506-518. https://doi.org/10.1016/j.jcis.2019.09.045

[5] H.Q. Wu, C.C. Wang, Biodegradable smart nanogels: a new platform for targeting drug delivery and biomedical diagnostics, Langmuir 32(25) (2016) 6211-6225. https://doi.org/10.1021/acs.langmuir.6b00842

[6] Z. Wang, R.X. Zhang, C. Zhang, C. Dai, X. Ju, R. He, Fabrication of stable and self-assembling rapeseed protein nanogel for hydrophobic curcumin delivery, J. Agric. Food Chem. 67(3) (2019) 887-894. https://doi.org/10.1021/acs.jafc.8b05572

[7] A. Araiza Calahorra, A. Sarkar, Pickering emulsion stabilized by protein nanogel particles for delivery of curcumin: Effects of pH and ionic strength on curcumin retention, Food Struct. 21 (2019) 100113. https://doi.org/10.1016/j.foostr.2019.100113

[8] M. Karimi, S. Bahrami, S.B. Ravari, P.S. Zangabad, H. Mirshekari, M. Bozorgomid, S. Shahreza, M. Sori, M.R. Hamblin, Albumin nanostructures as advanced drug delivery

750 systems, Expert Opin. Drug Deliv. 13(11) (2016) 1609-1623.
751 https://doi.org/10.1080/17425247.2016.1193149
752 [9] J. Li, P. Yao, Self-assembly of ibuprofen and bovine serum albumin−dextran conjugates
753 leading to effective loading of the drug, Langmuir 25(11) (2009) 6385-6391.
754 https://doi.org/10.1021/la804288u
755 [10] W. Chen, S. Zhou, L. Ge, W. Wu, X. Jiang, Translatable high drug loading drug delivery
756 systems based on biocompatible polymer nanocarriers, Biomacromolecules 19(6) (2018)
757 1732-1745. https://doi.org/10.1021/acs.biomac.8b00218
758 [11] Y. Sun, Y. Huang, Disulfide-crosslinked albumin hydrogels, J. Mater. Chem. B 4(16)
759 (2016) 2768-2775. https://doi.org/10.1039/C6TB00247A
760 [12] X. Liu, Y.L. Hsieh, Amphiphilic and amphoteric aqueous soy protein colloids and their
761 cohesion and adhesion to cellulose, Ind. Crops Prod. 144 (2020) 112041.
762 https://doi.org/10.1016/j.indcrop.2019.112041
763 [13] R.P. Das, B.G. Singh, A. Kunwar, M.V. Ramani, G.V. Subbaraju, P.A. Hassan, K.I.
764 Priyadarsini, Tuning the binding, release and cytotoxicity of hydrophobic drug by bovine
765 serum albumin nanoparticles: Influence of particle size, Colloids Surf. B. Biointerfaces 158
766 (2017) 682-688. https://doi.org/10.1016/j.colsurfb.2017.07.048
767 [14] F.P. Chen, S.Y. Ou, C.H. Tang, Core–shell soy protein–soy polysaccharide complex
768 (nano)particles as carriers for improved stability and sustained release of curcumin, J. Agric.
769 Food Chem. 64(24) (2016) 5053-5059. https://doi.org/10.1021/acs.jafc.6b01176
770 [15] T. del Castillo Santaella, J. Maldonado-Valderrama, J.A. Molina Bolivar, F. Galisteo
771 Gonzalez, Effect of cross-linker glutaraldehyde on gastric digestion of emulsified albumin,
772 Colloids Surf. B. Biointerfaces 145 (2016) 899-905.
773 https://doi.org/10.1016/j.colsurfb.2016.06.014

774 [16] K. Feng, C. Li, Y.S. Wei, M.H. Zong, H. Wu, S.Y. Han, Development of a
775 polysaccharide based multi-unit nanofiber mat for colon-targeted sustained release of salmon
776 calcitonin, J. Colloid Interface Sci. 552 (2019) 186-195.
777 https://doi.org/10.1016/j.jcis.2019.05.037
778 [17] M. Nooshkam, M. Varidi, Maillard conjugate-based delivery systems for the
779 encapsulation, protection, and controlled release of nutraceuticals and food bioactive
780 ingredients: A review, Food Hydrocoll. 100 (2020) 105389.
781 https://doi.org/10.1016/j.foodhyd.2019.105389
782 [18] J. Feng, S. Wu, H. Wang, S. Liu, Improved bioavailability of curcumin in ovalbumin-
783 dextran nanogels prepared by Maillard reaction, J. Funct. Foods 27 (2016) 55-68.
784 https://doi.org/10.1016/j.jff.2016.09.002
785 [19] Z. Wei, Q. Huang, Assembly of protein–polysaccharide complexes for delivery of
786 bioactive ingredients: A perspective paper, J. Agric. Food Chem. 67(5) (2019) 1344-1352.
787 https://doi.org/10.1021/acs.jafc.8b06063
788 [20] T.D. Clemons, R. Singh, A. Sorolla, N. Chaudhari, A. Hubbard, K.S. Iyer, Distinction
789 between active and passive targeting of nanoparticles dictate their overall therapeutic efficacy,
790 Langmuir 34(50) (2018) 15343-15349. https://doi.org/10.1021/acs.langmuir.8b02946
791 [21] G. Yang, S. Fu, W. Yao, X. Wang, Q. Zha, R. Tang, Hyaluronic acid nanogels prepared
792 via ortho ester linkages show pH-triggered behavior, enhanced penetration and antitumor
793 efficacy in 3-D tumor spheroids, J. Colloid Interface Sci. 504 (2017) 25-38.
794 https://doi.org/10.1016/j.jcis.2017.05.033
795 [22] P.K. Borah, M. Rappolt, R.K. Duary, A. Sarkar, Effects of folic acid esterification on the
796 hierarchical structure of amylopectin corn starch, Food Hydrocoll. 86 (2019) 162-171.
797 https://doi.org/10.1016/j.foodhyd.2018.03.028

798 [23] W. Shi, Y. Wang, H. Zhang, Z. Liu, Z. Fei, Probing deep into the binding mechanisms of
799 folic acid with α-amylase, pepsin and trypsin: An experimental and computational study,
800 Food Chem. 226 (2017) 128-134. https://doi.org/10.1016/j.foodchem.2017.01.054
801 [24] P.K. Borah, A. Sarkar, R.K. Duary, Water-soluble vitamins for controlling starch
802 digestion: Conformational scrambling and inhibition mechanism of human pancreatic α-
803 amylase by ascorbic acid and folic acid, Food Chem. 288 (2019) 395-404.
804 https://doi.org/10.1016/j.foodchem.2019.03.022
805 [25] P.K. Borah, M. Rappolt, R.K. Duary, A. Sarkar, Structurally induced modulation of in
806 vitro digestibility of amylopectin corn starch upon esterification with folic acid, Int. J. Biol.
807 Macromol. 129 (2019) 361-369. https://doi.org/10.1016/j.ijbiomac.2019.02.051
808 [26] T. Witt, R.G. Gilbert, Causal relations between structural features of amylopectin, a
809 semicrystalline hyperbranched polymer, Biomacromolecules 15(7) (2014) 2501-2511.
810 https://doi.org/10.1021/bm500353e
811 [27] C. Schüll, H. Frey, Grafting of hyperbranched polymers: From unusual complex polymer
812 topologies to multivalent surface functionalization, Polymer 54(21) (2013) 5443-5455.
813 https://doi.org/10.1016/j.polymer.2013.07.065
814 [28] A. Araiza Calahorra, M. Akhtar, A. Sarkar, Recent advances in emulsion-based delivery
815 approaches for curcumin: From encapsulation to bioaccessibility, Trends Food Sci. Technol.
816 71 (2018) 155-169. https://doi.org/10.1016/j.tifs.2017.11.009
817 [29] D. Bajani, J. Dey, Y. Rajesh, S. Bandyopadhyay, M. Mandal, Spontaneous vesicle
818 formation by γ-aminobutyric acid derived steroidal surfactant: Curcumin loading, cytotoxicity
819 and cellular uptake studies, J. Colloid Interface Sci. 507 (2017) 1-10.
820 https://doi.org/10.1016/j.jcis.2017.07.108

821 [30] W. Yang, M. Hattori, T. Kawaguchi, K. Takahashi, Properties of starches conjugated
822 with lysine and poly(lysine) by the maillard reaction, J. Agric. Food Chem. 46(2) (1998) 442-
823 445. https://doi.org/10.1021/jf970515i
824 [31] Y. Fan, J. Yi, Y. Zhang, W. Yokoyama, Fabrication of curcumin-loaded bovine serum
825 albumin (BSA)-dextran nanoparticles and the cellular antioxidant activity, Food Chem. 239
826 (2018) 1210-1218. https://doi.org/10.1016/j.foodchem.2017.07.075
827 [32] S. Buwalda, A. Al Samad, A. El Jundi, A. Bethry, Y. Bakkour, J. Coudane, B. Nottelet,
828 Stabilization of poly(ethylene glycol)-poly(ε-caprolactone) star block copolymer micelles via
829 aromatic groups for improved drug delivery properties, J. Colloid Interface Sci. 514 (2018)
830 468-478. https://doi.org/10.1016/j.jcis.2017.12.057
831 [33] I. Puskás, A. Szemjonov, É. Fenyvesi, M. Malanga, L. Szente, Aspects of determining
832 the molecular weight of cyclodextrin polymers and oligomers by static light scattering,
833 Carbohydr. Polym. 94(1) (2013) 124-128. https://doi.org/10.1016/j.carbpol.2013.01.025
834 [34] L. Whitmore, B.A. Wallace, Protein secondary structure analyses from circular
835 dichroism spectroscopy: Methods and reference databases, Biopolymers 89(5) (2008) 392-
836 400. https://doi.org/10.1002/bip.20853
837 [35] H. Yang, P. Wen, K. Feng, M.H. Zong, W.Y. Lou, H. Wu, Encapsulation of fish oil in a
838 coaxial electrospun nanofibrous mat and its properties, RSC Adv. 7(24) (2017) 14939-14946.
839 https://doi.org/10.1039/C7RA00051K
840 [36] M. Minekus, M. Alminger, P. Alvito, S. Ballance, T. Bohn, C. Bourlieu, F. Carrière, R.
841 Boutrou, M. Corredig, D. Dupont, C. Dufour, L. Egger, M. Golding, S. Karakaya, B. Kirkhus,
842 S. Le Feunteun, U. Lesmes, A. Macierzanka, A. Mackie, S. Marze, D.J. McClements, O.
843 Ménard, I. Recio, C.N. Santos, R.P. Singh, G.E. Vegarud, M.S.J. Wickham, W. Weitschies,
844 A. Brodkorb, A standardised static in vitro digestion method suitable for food – an

845 international consensus, Food Funct. 5(6) (2014) 1113-1124.
846 https://doi.org/10.1039/C3FO60702J
847 [37] A. Kunwar, A. Barik, K. Priyadarsini, R. Pandey, Absorption and fluorescence studies of
848 curcumin bound to liposome and living cells, BARC newsletter 285 (2007) 213-218.
849 [38] D. Baskić, S. Popović, P. Ristić, N.N. Arsenijević, Analysis of cycloheximide-induced
850 apoptosis in human leukocytes: Fluorescence microscopy using annexin V/propidium iodide
851 versus acridin orange/ethidium bromide, Cell Biol. Int. 30(11) (2006) 924-932.
852 https://doi.org/10.1016/j.cellbi.2006.06.016
853 [39] M. Khoder, K.H. Gbormoi, A. Ryan, A. Karam, G.R. Alany, Potential use of the
854 Maillard reaction for pharmaceutical applications: Gastric and intestinal controlled release
855 alginate-albumin beads, Pharmaceutics 11(2) (2019) 83-94.
856 https://doi.org/10.3390/pharmaceutics11020083
857 [40] A. Bhattacherjee, K. Dhara, A.S. Chakraborti, Bimolecular interaction of argpyrimidine
858 (a Maillard reaction product) in in vitro non-enzymatic protein glycation model and its
859 potential role as an antiglycating agent, Int. J. Biol. Macromol. 102 (2017) 1274-1285.
860 https://doi.org/10.1016/j.ijbiomac.2017.04.108
861 [41] W. Jian, J. He, Y. Sun, J. Pang, Comparative studies on physicochemical properties of
862 bovine serum albumin-glucose and bovine serum albumin-mannose conjugates formed via
863 Maillard reaction, LWT - Food Sci. Technol. 69 (2016) 358-364.
864 https://doi.org/10.1016/j.lwt.2015.11.061
865 [42] A.K. Anal, S. Shrestha, M.B. Sadiq, Biopolymeric-based emulsions and their effects
866 during processing, digestibility and bioaccessibility of bioactive compounds in food systems,
867 Food Hydrocoll. 87 (2019) 691-702. https://doi.org/10.1016/j.foodhyd.2018.09.008

868 [43] H.P. Erickson, Size and shape of protein molecules at the nanometer level determined by
869 sedimentation, gel filtration, and electron microscopy, Biol. Proced. Online 11(1) (2009) 32.
870 https://doi.org/10.1007/s12575-009-9008-x
871 [44] C. Fong, T. Le, C.J. Drummond, Lyotropic liquid crystal engineering–ordered
872 nanostructured small molecule amphiphile self-assembly materials by design, Chem. Soc.
873 Rev. 41(3) (2012) 1297-1322. https://doi.org/10.1039/C1CS15148G
874 [45] A. Benichou, A. Aserin, R. Lutz, N. Garti, Formation and characterization of amphiphilic
875 conjugates of whey protein isolate (WPI)/xanthan to improve surface activity, Food
876 Hydrocoll. 21(3) (2007) 379-391. https://doi.org/10.1016/j.foodhyd.2006.04.013
877 [46] P.V.F. Lemos, L.S. Barbosa, I.G. Ramos, R.E. Coelho, J.I. Druzian, Characterization of
878 amylose and amylopectin fractions separated from potato, banana, corn, and cassava starches,
879 Int. J. Biol. Macromol. 132 (2019) 32-42. https://doi.org/10.1016/j.ijbiomac.2019.03.086
880 [47] E. Adal, A. Sadeghpour, S. Connell, M. Rappolt, E. Ibanoglu, A. Sarkar, Heteroprotein
881 complex formation of bovine lactoferrin and pea protein isolate: A multiscale structural
882 analysis, Biomacromolecules 18(2) (2017) 625-635.
883 https://doi.org/10.1021/acs.biomac.6b01857
884 [48] G. Güler, M.M. Vorob'ev, V. Vogel, W. Mäntele, Proteolytically-induced changes of
885 secondary structural protein conformation of bovine serum albumin monitored by Fourier
886 transform infrared (FT-IR) and UV-circular dichroism spectroscopy, Spectrochim. Acta A
887 Mol. Biomol. Spectrosc. 161 (2016) 8-18. https://doi.org/10.1016/j.saa.2016.02.013
888 [49] G. Su, L. Li, D. Zhao, B. Li, X. Zhang, The digestibility of hydrothermally-treated
889 bovine serum albumin glycated by glyoxal, RSC Adv. 8(63) (2018) 35870-35877.
890 https://doi.org/10.1039/C8RA02585A

[50] J. Liu, H. Jing, Glycation of bovine serum albumin with monosaccharides inhibits heat-induced protein aggregation, RSC Adv. 6(116) (2016) 115183-115188. https://doi.org/10.1039/C6RA24580C

[51] I.J. Joye, D.J. McClements, Biopolymer-based nanoparticles and microparticles: Fabrication, characterization, and application, Curr. Opin. Colloid Interface Sci. 19(5) (2014) 417-427. https://doi.org/10.1016/j.cocis.2014.07.002

[52] D.N. Benoit, H. Zhu, M.H. Lilierose, R.A. Verm, N. Ali, A.N. Morrison, J.D. Fortner, C. Avendano, V.L. Colvin, Measuring the grafting density of nanoparticles in solution by analytical ultracentrifugation and total organic carbon analysis, Anal. Chem. 84(21) (2012) 9238-9245. https://doi.org/10.1021/ac301980a

[53] C.M. Durrani, A.M. Donald, Shape, molecular weight distribution and viscosity of amylopectin in dilute solution, Carbohydr. Polym. 41(2) (2000) 207-217. https://doi.org/10.1016/S0144-8617(99)00070-3

[54] X. Liu, X. Xiao, P. Liu, L. Yu, M. Li, S. Zhou, F. Xie, Shear degradation of corn starches with different amylose contents, Food Hydrocoll. 66 (2017) 199-205. https://doi.org/10.1016/j.foodhyd.2016.11.023

[55] R. Shi, Z. Zhang, Q. Liu, Y. Han, L. Zhang, D. Chen, W. Tian, Characterization of citric acid/glycerol co-plasticized thermoplastic starch prepared by melt blending, Carbohydr. Polym. 69(4) (2007) 748-755. https://doi.org/10.1016/j.carbpol.2007.02.010

[56] T.A. Grünewald, A. Lassenberger, P.D.J. van Oostrum, H. Rennhofer, R. Zirbs, B. Capone, I. Vonderhaid, H. Amenitsch, H.C. Lichtenegger, E. Reimhult, Core–Shell Structure of Monodisperse Poly(ethylene glycol)-Grafted Iron Oxide Nanoparticles Studied by Small-Angle X-ray Scattering, Chem. Mater. 27(13) (2015) 4763-4771. 10.1021/acs.chemmater.5b01488

915 [57] P.K. Borah, S.C. Deka, R.K. Duary, Effect of repeated cycled crystallization on
916 digestibility and molecular structure of glutinous Bora rice starch, Food Chem. 223 (2017) 31-
917 39. https://doi.org/10.1016/j.foodchem.2016.12.022
918 [58] S. Wong, J. Zhao, C. Cao, C.K. Wong, R.P. Kuchel, S. De Luca, J.M. Hook, C.J. Garvey,
919 S. Smith, J. Ho, M.H. Stenzel, Just add sugar for carbohydrate induced self-assembly of
920 curcumin, Nat. Commun. 10(1) (2019) 582. https://doi.org/10.1038/s41467-019-08402-y
921 [59] C. Hao, G. Xu, T. Wang, Z. Lv, K. Zhu, B. Li, S. Chen, R. Sun, The mechanism of the
922 interaction between curcumin and bovine serum albumin using fluorescence spectrum, Russ.
923 J. Phys. Chem. B 11(1) (2017) 140-145. https://doi.org/10.1134/S1990793117010043
924 [60] A.A. Thorat, S.V. Dalvi, Particle formation pathways and polymorphism of curcumin
925 induced by ultrasound and additives during liquid antisolvent precipitation, CrystEngComm
926 16(48) (2014) 11102-11114. https://doi.org/10.1039/C4CE02021A
927 [61] J. Li, G.H. Shin, I.W. Lee, X. Chen, H.J. Park, Soluble starch formulated nanocomposite
928 increases water solubility and stability of curcumin, Food Hydrocoll. 56 (2016) 41-49.
929 https://doi.org/10.1016/j.foodhyd.2015.11.024
930 [62] R. Jagannathan, P.M. Abraham, P. Poddar, Temperature-dependent spectroscopic
931 evidences of curcumin in aqueous medium: A mechanistic study of its solubility and stability,
932 The Journal of Physical Chemistry B 116(50) (2012) 14533-14540. 10.1021/jp3050516
933 [63] M.M. Yallapu, B.K. Gupta, M. Jaggi, S.C. Chauhan, Fabrication of curcumin
934 encapsulated PLGA nanoparticles for improved therapeutic effects in metastatic cancer cells,
935 J. Colloid Interface Sci. 351(1) (2010) 19-29. https://doi.org/10.1016/j.jcis.2010.05.022
936 [64] P. Sanphui, G. Bolla, Curcumin, a biological wonder molecule: A crystal engineering
937 point of view, Cryst. Growth Des. 18(9) (2018) 5690-5711.
938 https://doi.org/10.1021/acs.cgd.8b00646

939 [65] S. Elmore, Apoptosis: A review of programmed cell death, Toxicol. Pathol. 35(4) (2007)
940 495-516. https://doi.org/10.1080/01926230701320337
941 [66] C.P. Leamon, P.S. Low, Delivery of macromolecules into living cells: a method that
942 exploits folate receptor endocytosis, Proc. Natl. Acad. Sci. 88(13) (1991) 5572.
943 https://doi.org/10.1073/pnas.88.13.5572
944 [67] G.H. Shin, J. Li, J.H. Cho, J.T. Kim, H.J. Park, Enhancement of curcumin solubility by
945 phase change from crystalline to amorphous in Cur-TPGS nanosuspension, J. Food Sci. 81(2)
946 (2016) N494-N501. https://doi.org/10.1111/1750-3841.13208
947

CRediT author statement

Pallab Kumar Borah: Conceptualization; Data curation; Validation; Formal analysis; Visualization; Funding acquisition; Writing- Original draft preparation. **Anindhya Sundar Das:** Data curation; Validation; Formal analysis; Visualization; Writing- Original draft preparation. **Rupak Mukhopadhyay:** Formal analysis; Funding acquisition; Resources; Writing - review & editing. **Anwesha Sarkar:** Conceptualization; Supervision; Formal analysis; Resources; Writing - review & editing. **Raj Kumar Duary:** Conceptualization; Supervision; Formal analysis; Resources; Writing - review & editing.

957

Supplementary material

959

Macromolecular design of folic acid functionalized amylopectin-albumin core-shell nanogels for improved physiological stability and colon cancer cell targeted delivery of curcumin

963

964 Pallab Kumar Borah[a, b], Anindhya Sundar Das[c], Rupak Mukhopadhyay[c], Anwesha Sarkar[b]†,
965 Raj Kumar Duary[a]*

966

967 [a] *Department of Food Engineering and Technology, School of Engineering, Tezpur*
968 *University, 784 028, India*

969 [b] *Food Colloids and Bioprocessing Group, School of Food Science and Nutrition, University*
970 *of Leeds, LS2 9JT, United Kingdom*

971 [c] *Department of Molecular Biology and Biotechnology, School of Sciences, Tezpur University,*
972 *784 028, India*

973

974 **Email:** pallab@tezu.ernet.in; dasanindhyasundar@gmail.com; mrupak@tezu.ernet.in;
975 A.Sarkar@leeds.ac.uk†; duary@tezu.ernet.in*

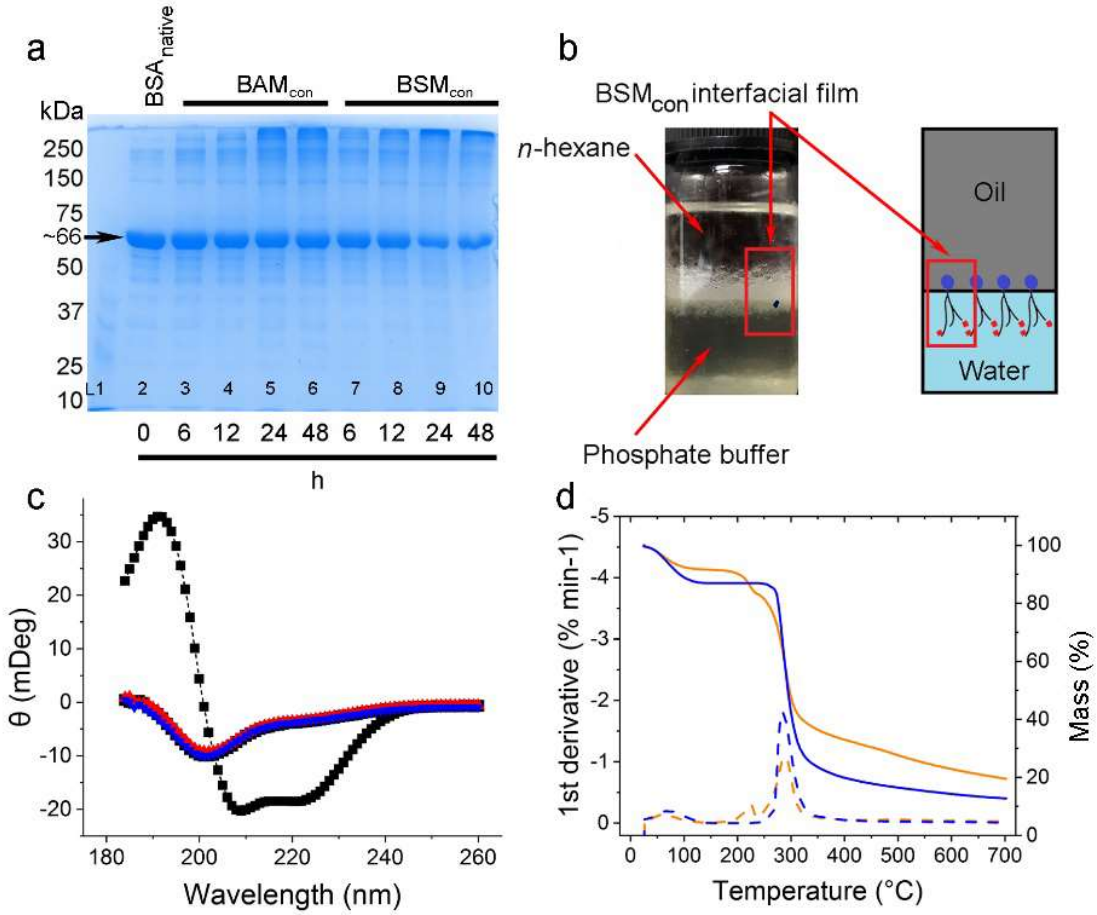

Figure S1. SDS-PAGE electrogram of BSA_{native}, BAM_{con} and BSM_{con} at different Maillard reaction times (a). Visual image of the interfacial film of amphiphilic BSM_{con} at the n-hexane/phosphate buffer (10 mM, pH 7.4) interface (left) and schematic illustration of the amphiphile at the oil/water interface (right) (b). Circular dichroism spectra of BSA_{native} (black, ■) protein and BSM (blue, ▼), BAM (red, ▲), and BSA (black, ●) nanogels dispersed in 10 mM phosphate buffer at pH 7.4 (c). Solid lines and dashed lines (SF20 (orange) and ACS (blue)) represent the TGA and DTG thermograms, respectively (d).

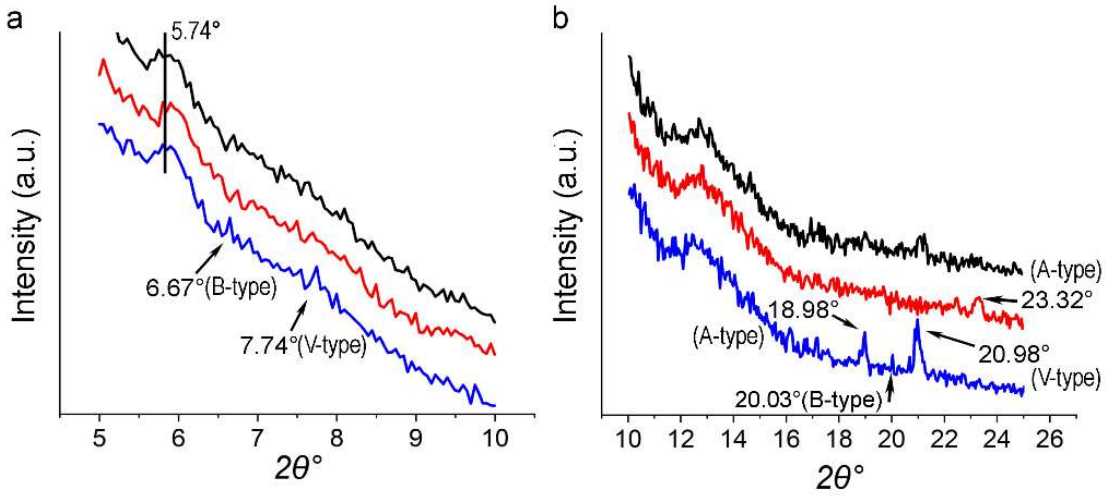

Figure S2. XRD diffractograms of BSM (blue), BAM (red), and BSA (black) at 2θ, 5-10° (a) and 10-25° (b), respectively. Arrows and values indicate diffraction angles and polymorphism types. The diffractograms are offset vertically for clarity.

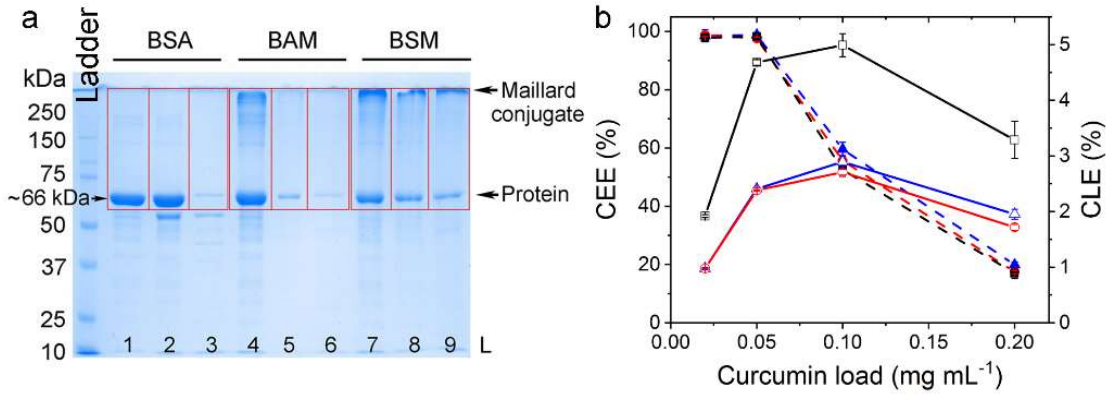

990

991 Figure S3. SDS-PAGE electrogram of *in vitro* oral-gastrointestinal digesta as in Figure 5. Red
992 enclosures identify zones used for images analysis of the individual digesta. Lanes L1: BSA,
993 0 min (sample, oral-gastrointestinal digestion time), L2: BSA, 30 min; L3: BSA, 300 min, L4:
994 BAM, 0 min, L5: BAM, 30 min, L6: BAM, 300 min, L7: BSM, 0 min, L8: BSM, 30 min, L9:
995 BSM, 300 min (a). Curcumin encapsulation efficiency (*CEE*, solid symbols and dashed line)
996 and curcumin loading efficiency (*CLE*, open symbols and solid line) as a function of
997 curcumin load used for the preparation of the BSM_{cur} (blue, ▲, △), BAM_{cur} (red, ●, ○), and
998 BSA_{cur} (black, ■, □) nanogels. Error bars represent standard deviations of independent
999 analysis, $n = 3$ (b).

1000

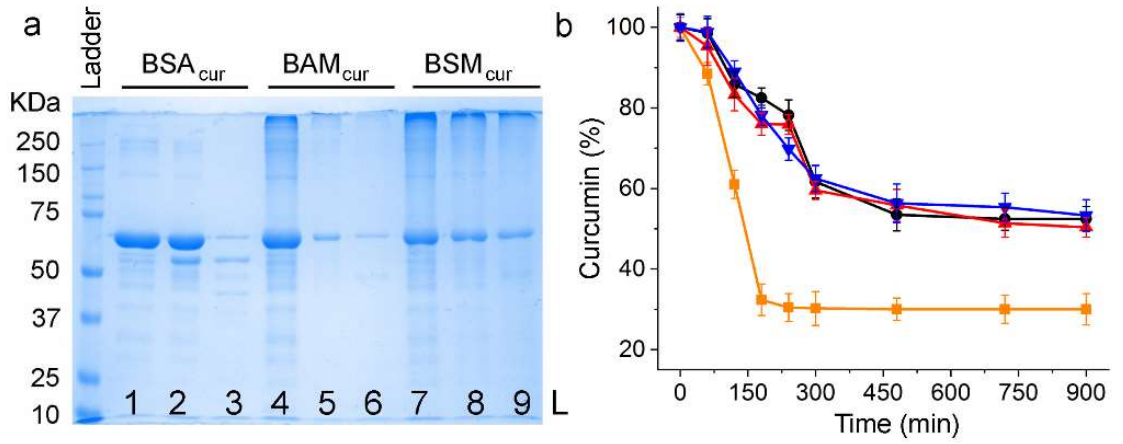

Figure S4. SDS-PAGE electrogram of *in vitro* oral-gastrointestinal digesta of curcumin encapsulated nanogels (curcumin load, 0.05 mg mL^{-1}), Lanes L 1: BSA_{cur}, 0 min (sample, oral-gastrointestinal digestion time), L 2: BSA_{cur}, 30 min; L 3: BSA_{cur}, 300 min, L 4: BAM_{cur}, 0 min, L 5: BAM_{cur}, 30 min, L 6: BAM_{cur}, 300 min, L 7: BSM_{cur}, 0 min, L 8: BSM_{cur}, 30 min, L 9: BSM_{cur}, 300 min. (a). Degradation of curcumin (curcumin load, 0.05 mg mL^{-1}) at pH 7.4 under direct light (1000 lumen); free curcumin (orange, ■), BSM_{cur} (blue, ▼), BAM_{cur} (red, ▲), and BSA_{cur} (black, ●) (b). Error bars represent standard deviations of independent analysis, $n = 3$.

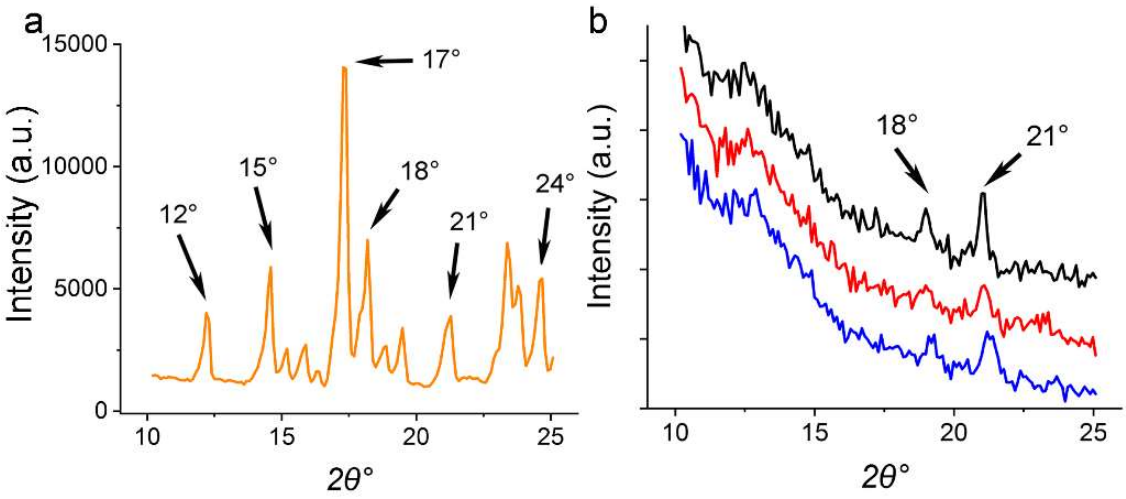

Figure S5. XRD diffractograms of curcumin (orange) (a), and BSM_{cur} (blue), BAM_{cur} (red), and BSA_{cur} (black) at curcumin load of 0.05 mg mL^{-1}. Arrows and values indicate diffraction angles. The diffractograms are offset vertically for clarity (b).

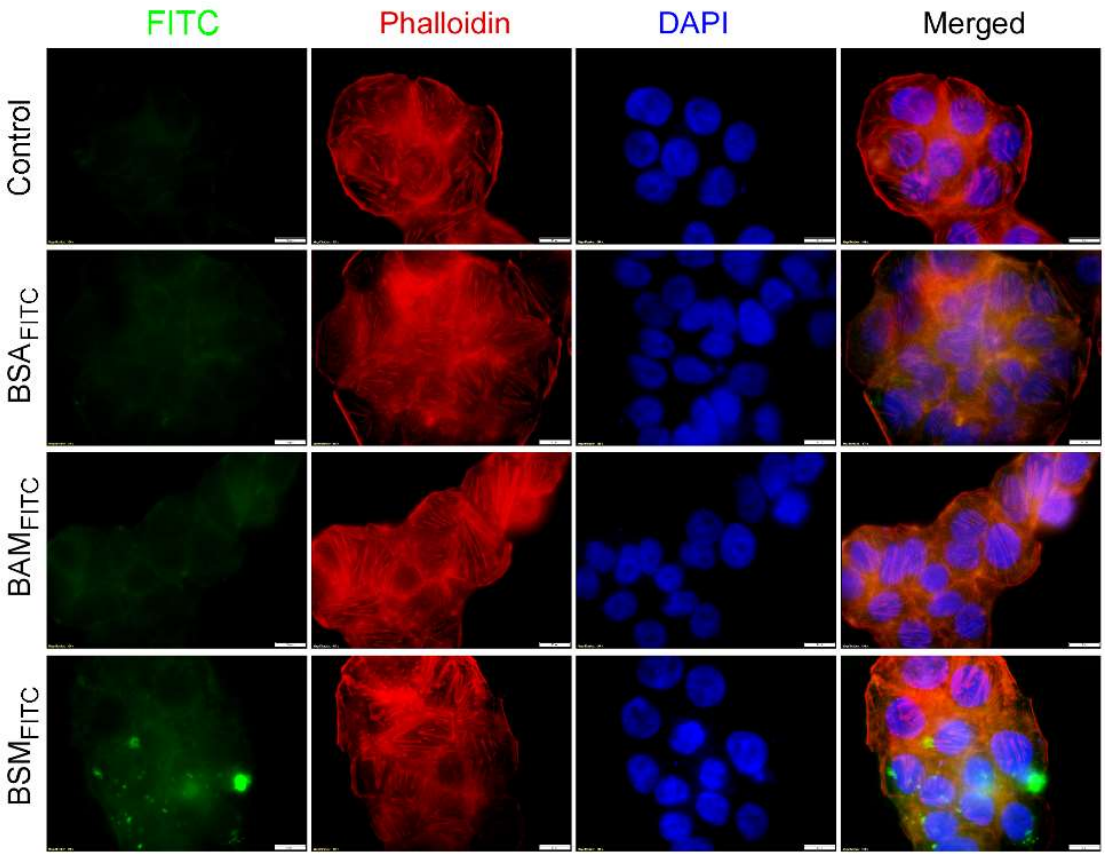

Figure S6. Fluorescence micrographs of folate-receptor positive HT29 cells treated with FITC-tagged nanogels. The control contained no nanogels and only phosphate buffer 10 mM at pH 7.4. Scale bars are 10 μm.

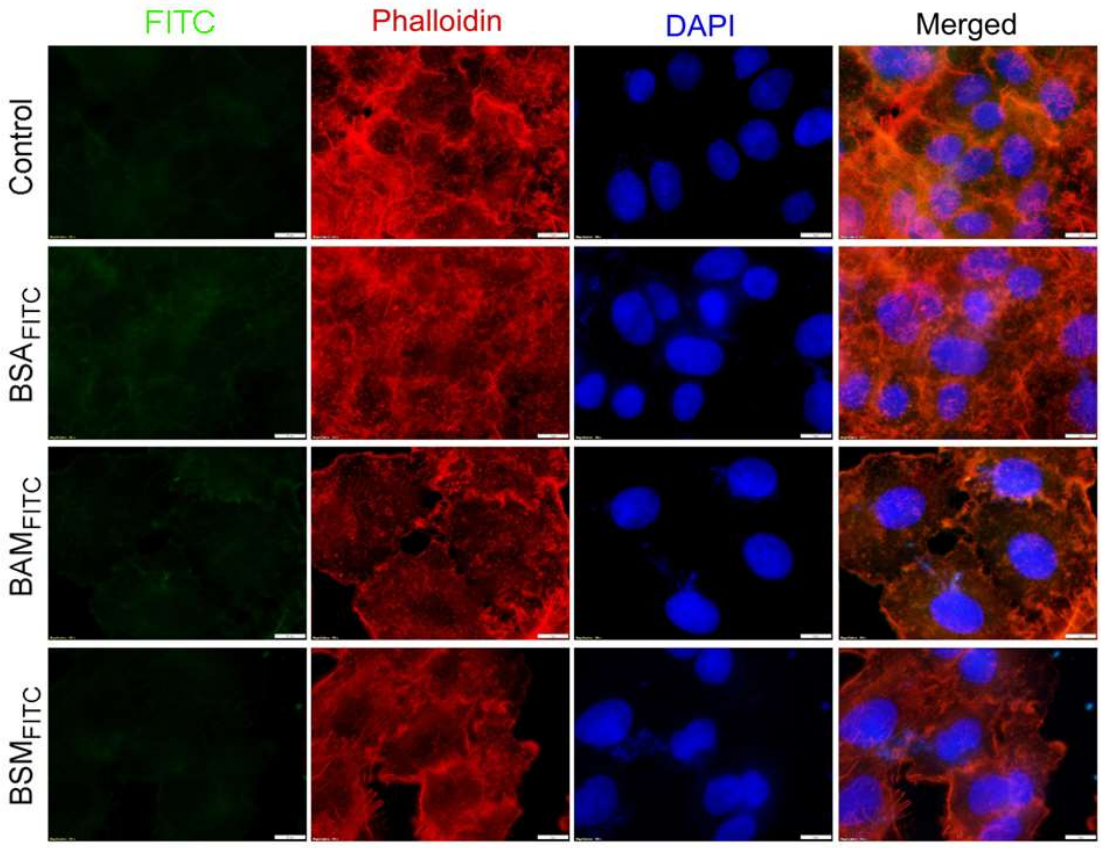

Figure S7. Fluorescence micrographs of folate-receptor negative A549 cells treated with FITC-tagged nanogels. The control contained no nanogels and only phosphate buffer 10 mM at pH 7.4. Scale bars are 10 μm.

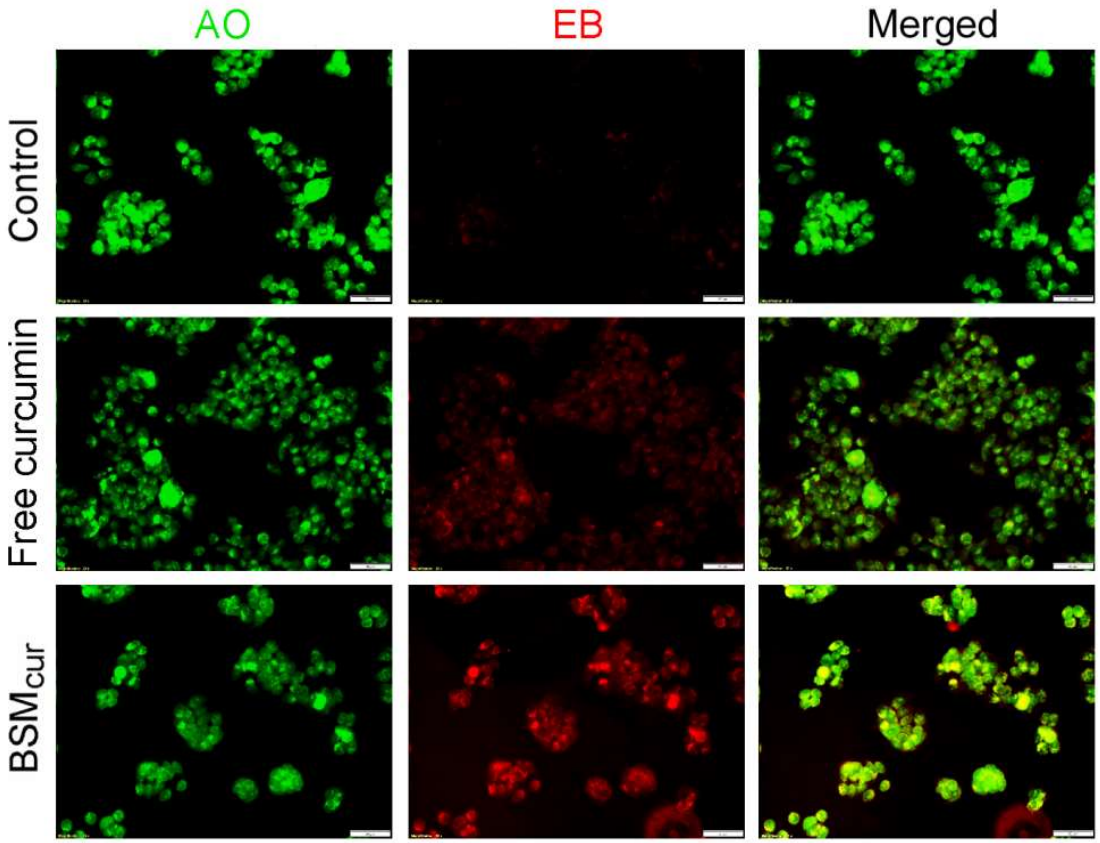

Figure S8. AO/EB assay of free curcumin (0.05 mg mL^{-1}) and curcumin encapsulated BSM_{cur} nanogels (0.05 mg mL^{-1} curcumin load) treated with folate-receptor positive HT29 cells. The control contained only phosphate buffer 10 mM at pH 7.4. Scale bars are 50 μm.

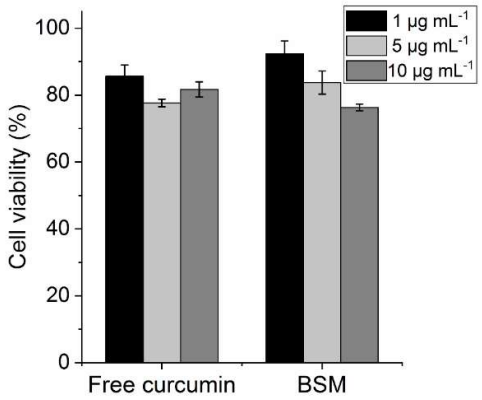

Figure S9. MTT assay showing the viability of HT29 cells after exposure to increasing load of free curcumin and BSM nanogels (1 - 10 μg mL^{-1}, respectively) for 24 h. Error bars represent standard deviations of independent analysis, $n = 3$.